

Probabilistic State Estimation Under Varying Loading States via the Integration of Time-Varying Autoregressive and Gaussian Process Models

Ahmad Amer¹ , Shabbir Ahmed²
 and Fotis Kopsaftopoulos³ 

Abstract

In this work, probabilistic damage quantification under varying loading conditions in a non-stationary, guided-wave environment is being tackled via the synergistic integration between Time-varying Autoregressive (TAR) models and Gaussian Process regression models (GPRMs). Applying these TAR-GPRMs onto an aluminum coupon with simulated damage under different loading conditions fitted with piezoelectric sensors/actuators, the TAR models show the capability of capturing the non-stationarity in the ultrasonic guided-wave signals generated by the actuators under varying plate-loading conditions. They also provide insights to the maintainer by showing when in time the guided-wave time series deviate the most. In order to take advantage of that, a time instant selection algorithm was developed to allow flexibility in choosing the time instant(s) at which probabilistic damage quantification should be done. Finally, this quantification task is tackled by GPRMs, in which multiple GPRMs are trained using the TAR model parameters under varying conditions, and then used to predict damage size and/or loading state. While this framework is much more powerful in terms of tapping into the dynamics of how guided-waves change with varying conditions compared to simpler forms of GPRMs (such as damage index-trained GPRMs), training of TAR-GPRMs is far more complex. The advantages and challenges associated with the proposed TAR-GPRM approach is presented herein along with potential open areas for research in this regard.

Keywords

Probabilistic SHM, damage quantification, Gaussian Process, time-varying autoregressive, guided waves

Introduction

In many engineering case studies, safety is a major driver for the business case.^{1–3} The need for prolonging operational life, or simply limiting maintenance shutdowns has created a global search for better frameworks that allow for enhanced life-cycle management of engineering structures.^{4–6} At the center of these global endeavors is structural health monitoring (SHM) research,⁷ which has brought about a plethora of techniques that allow for the detection, localization, and quantification of damage within engineering components. In particular, active-sensing, guided-wave SHM frameworks have seen a lot of interest throughout the past decade due to their sensitivity to damage at its early stages, that is, damage that is small enough to not affect system dynamics.^{8–11} In this context, the

sensitivity of active-sensing, guided-wave SHM networks has proven to be prone to false alarms and vulnerable to the effects of operational and environmental conditions.^{12–15} Thus, most research endeavors

¹Probabilistic Design and Materials Informatics Team, General Electric Research, Niskayuna, NY, USA

²Structures and Composites Laboratory, Department of Aeronautics and Astronautics, Stanford University, Stanford CA, USA

³Intelligent Structural Systems Laboratory, Department of Mechanical, Aerospace and Nuclear Engineering, Rensselaer Polytechnic Institute, Troy, NY, USA

Corresponding author:

Ahmad Amer, Probabilistic Design and Materials Informatics Team, General Electric Research, 1 Research Cr, Niskayuna, NY 12309-1027, USA.

Email: ahmad.amer@ge.com

throughout the active-sensing, guided-wave SHM community have been directed toward devising techniques that can do accurate damage detection, localization, and quantification under operational and environmental uncertainty.

Toward this end, the problem of varying environmental and operational conditions has been treated using different approaches in the literature. On one side, compensation-based techniques, which use physics-based models have been extensively used. Techniques as optimal baseline subtraction,^{16,17} baseline signal stretching,^{18,19} compressed sensing,²⁰ matching pursuit,^{21–23} and time warping²⁴ have been suggested in this sense in order to compensate for the effects of varying conditions on guided-wave signals. Although the family of condition-compensation techniques has proven to be efficient in eliminating the effects of temperature and loading on guided-wave signals, these techniques still face issues when it comes to large variations in either condition.²⁵ In addition, uncertainty due to varying conditions may not always come solely from temperature or load variations,^{15,26} and other sources of uncertainty need to be included in the analysis for accurate and robust damage identification. Thus, many researchers have looked into using purely data-driven techniques in order to model or eliminate the effects of varying conditions on guided-wave propagation. Techniques such as principal component analysis and its variants,^{27–30} artificial neural networks,^{10,31,32} support vector machines,^{33,34} discriminant approaches,³⁵ and baseline-free techniques^{36–38} have been used as non-probabilistic efforts toward decoupling the effects of damage from those of varying conditions. Although these techniques have shown promise in treating the problem of varying conditions, they lack a proper framework for modeling the uncertainties associated with guided-wave signals and thus do not generalize well beyond the experimental sets on which they are used or trained, especially for complex components.

To bypass the shortcomings of the above methods, probabilistic techniques such as Gaussian mixture models,^{39,40} hidden Markov models,⁴¹ and Bayesian hierarchical models^{42,43} were proposed for modeling the uncertainties associated with guided-wave propagation within the framework of damage identification under varying operational and environmental conditions.⁴⁴ One family of probabilistic techniques that has seen a lot of traction within the vibration-based SHM communities is the family of time series models (see for instance, literatures^{45–47}). Like the other probabilistic techniques, these models readily provide estimation uncertainties over predictions. On the other hand, unlike other probabilistic techniques, some time series models have the capability to tackle the problem of time-varying dynamics (non-stationarity),^{48–50} which is

a well-known problem in vibration signals. This latter advantage has made time series models very popular when it comes to modeling system response under operational and environmental uncertainty.⁵¹ When it comes to active-sensing, guided-wave networks, it is well known that the effects of varying operational and environmental conditions are time-varying.⁴⁰ Thus, the application of time-varying time series models to active-sensing, guided-wave SHM frameworks is very promising in tackling the problem of damage detection and quantification under varying conditions. However, even for vibration-based SHM, with substantial experimental uncertainty (e.g., widely varying conditions), time series models can face challenges as evidenced by the very low type I error probability level that is required to bypass this issue.^{52,53} Although some workarounds have been proposed to model this experimental uncertainty (see for instance, literatures^{54,55}), just like most of the discussed techniques, these approaches still fall short when new sources of uncertainty which are not being used in building the original model, come up in the test data.⁵⁶ With the high sensitivity of guided waves to varying conditions, migrating time series models to guided-wave signals analysis is not a trivial task, and more sophisticated model structures will be required for tackling this problem.

One approach for solving this problem with time series models is their integration with Gaussian Process regression models (GPRMs). Indeed, GPRMs have seen a lot of traction within the vibration-based SHM community especially for modeling uncertainties that cannot be readily modeled by time series models.^{57–59} The main advantage of such models is their simplicity compared to other probabilistic techniques. Also, just like the latter, GPRMs can properly account for uncertainties within the training data regardless of their source (be it variations in loads, temperatures, humidity, material properties, etc.),⁶⁰ and thus elegantly provide “global” confidence bounds on damage identification. In particular, the integration of time series and Gaussian Process models (GPMs)^{61–63} have shown promise in modeling non-linear dynamics, as well as system response under different sources of variation. For instance, Fuentes et al.⁶⁴ used Gaussian Process (GPs) to propagate observation uncertainties (originating from varying conditions) from one time instant to another in an Autoregressive process for damage detection. Also modeling structural dynamics under varying environmental and operational conditions on a wind turbine blade, Avendano-Valencia et al. used time series models (vector⁶² and functionally pooled⁵⁶) models to model the short-term effects of varying conditions, and treated the parameters as Gaussian Processes for capturing the long-term effects. In a similar approach, Worden et al.⁶⁵ used GPs to model the

uncertainties in nonlinear autoregressive with exogenous input models, which are famous for constructing higher frequency response functions that properly capture dynamics of a nonlinear system. These endeavors in the vibration-based SHM literature demonstrate the potential of integrating GPs with time series models. However, no such integration frameworks exist in the literature for active-sensing, guided-wave networks. Thus, when it comes to the latter networks, the following tasks remain to be simultaneously tackled in the literature to achieve more accurate and robust damage identification in uncertain environments:

- Proper modeling of the time-varying effects of varying operational and environmental conditions on guided-wave signals
- Proper modeling of uncertainties within guided-wave signals, whether connected to the long-term effects of varying conditions, or other sources

To this end, the authors have used Gaussian Process regression and classification models in addressing the problem of probabilistic damage quantification under varying conditions^{14,25,66} within active-sensing, guided-wave SHM frameworks. In addition, the authors have also recently proposed integrating GPRMs with time series models⁶⁷ for combining the best of both frameworks: the wide uncertainty quantification of GPRMs and the capability of time-varying time series models for modeling non-stationary events. The work presented herein is an expansion of the latter work. The aim of the current study is to tackle the problem of modeling systems' time-varying response under varying operational conditions within the framework of active-sensing, guided-wave SHM. A framework integrating non-stationary time-series representations and GPRMs is proposed and critically assessed here in order to address the aforementioned tasks. The novelty in this work lies in the use of non-stationary models to model time-varying dynamics, as well as multi-input GPRMs to model system response under varying damage and load conditions (along with unknown experimental sources of variation). To the authors' best of knowledge, such a framework has not been applied before to guided-wave SHM problems. The proposed framework is applied to an aluminum (Al) coupon under varying damage and loading conditions.

The remaining part of the paper is organized as follows: the second section lays out the theoretical framework of the time series model (2.1) and GPRM (2.2) used herein. Then, after presenting the test setup in the third section, the results and their discussion are presented for one-dimensional and two-dimensional GPRMs in sections "Damage size quantification results"

and "Simultaneous damage size and load quantification results," respectively. Finally, the most important conclusions and suggestions for future work are outlined in the fifth section.

Background

Time-varying autoregressive models

Guided waves are inherently non-stationary due to their time-dependent (evolutionary) characteristics, as well as heavily influenced by environmental and operating conditions. The time-varying nature of wave propagation requires the use of corresponding time-varying non-parametric and/or parametric models.^{68–70} Stochastic parametric non-stationary (time-varying) models such as time-varying autoregressive (TAR) models or related types and their extensions have been mainly used in the context of random vibration analysis,^{68–70} with a detailed review presented in the study by Poulimenos and Fassois.⁶⁸ TAR models represent their conventional, stationary Autoregressive (AR) counterparts with the significant difference being that they allow their parameters to depend upon time and *adapt* based on the time-dependent nature of wave propagation.^{68,69} A TAR(*na*) model, with *na* designating its AR order, is thus of the form:

$$y[t] + \sum_{i=1}^{na} \alpha_i[t] \cdot y[t-i] = e[t] \quad \text{with } e[t] \sim \text{iid } \mathcal{N}(0, \sigma_e^2[t]) \quad (1)$$

with *t* designating discrete time, *y*[*t*] the time-varying wave propagation signal to be modeled, *e*[*t*] an (unobservable) uncorrelated (white) innovations sequence with zero mean and time-dependent variance $\sigma_e^2[t]$, and $\alpha_i[t]$, the model's time-dependent AR parameters. It is important to note here, that TAR models entertain simplicity in that there are no time-dependence "structures" imposed upon the time-dependent parameters, which leads to the parameters changing freely with time as will be shown later on.

Non-stationary TAR model identification. Given a single, *N*-sample-long, non-stationary signal record $\{y[1], \dots, y[N]\}$, the TAR identification problem may be stated as the problem of selecting the corresponding model structure and estimating the model parameters $\alpha_i[t]$ and the innovations variance $\sigma_e^2[t]$ that "best" fit the available measurements. A TAR model is parameterized via the AR vector $\Theta[t] = [\alpha_1[t] \ \alpha_2[t] \ \dots \ \alpha_{na}[t]]_{(na \times 1)}^T$ to be estimated based on the recorded non-stationary signal. The model identification problem is usually divided into two sub-problems: (i) *parameter*

estimation and (ii) *model structure selection*. In this thesis, model structure selection, where the order of the AR parameters is selected, was done by calculating the residual sum of squares (the sum of squares of the model's prediction errors—see below) and dividing it by the signal sum of squares (RSS/SSS). The model order that gave the smallest RSS/SSS was considered as the most “fitting” structure modeling the signals. Other techniques that can be applied to model structure selection are the Akaike and the Bayesian Information Criteria, or the maximum Gaussian log-likelihood.⁶⁸ As for parameter estimation, in this work, it was based on an exponentially weighted prediction error criterion (incorporating a “forgetting” factor)⁶⁸:

$$\hat{\boldsymbol{\theta}}[t] = \arg \min_{\boldsymbol{\theta}[t]} \sum_{\tau=1}^t \lambda^{t-\tau} e^2[\tau, \boldsymbol{\theta}^{\tau-1}], \quad (2)$$

such that

$$e[t, \boldsymbol{\theta}^{t-1}] \stackrel{\Delta}{=} y[t] - \sum_{i=1}^{na} \alpha_i[t-1] \cdot y[t-i] \approx e[t, \boldsymbol{\theta}^t] \quad (3)$$

Noting that $\lambda \in (0, 1)$ is called the *forgetting factor*, and sets how “fast” older error estimates are forgotten (the smaller it is, the less weight the older error estimates receive) through the weighing function $\lambda^{t-\tau}$. $e[t, \boldsymbol{\theta}^{t-1}]$ is the one-step ahead prediction at $t-1$ in the absence of knowledge of the parameter values at t as is normally required; the approximation in Equation (3) is true for slow parameter evolution. A recursive estimation scheme accomplished via the recursive maximum likelihood (RML) method^{68,70} is used in estimating the parameters $\boldsymbol{\theta}[t]$. In this scheme, the estimations are updated via:

$$\hat{\boldsymbol{\theta}}[t] = \hat{\boldsymbol{\theta}}[t-1] + \mathbf{k}[t] \cdot \hat{e}[t|t-1] \quad (4)$$

where

$$\Phi[t] = [-y[t-1] - y[t-2] \dots - y[t-na]]$$

and the gain $\mathbf{k}[t]$ is defined as:

$$\mathbf{k}[t] = \frac{\mathbf{P}[t-1] \cdot \Phi[t]}{\lambda + \Phi^T[t] \cdot \mathbf{P}[t-1] \cdot \Phi[t]} \quad (5)$$

where $\mathbf{P}[t]$ is the covariance matrix of the parameters at time t . The prediction error $\hat{e}[t|t-1]$ can be written as:

$$\hat{e}[t|t-1] = y[t] - \hat{y}[t|t-1] = y[t] - \Phi^T[t] \cdot \hat{\boldsymbol{\theta}}[t-1] \quad (6)$$

Finally, the covariance of the parameters can be updated through:

$$\mathbf{P}[t] = \frac{\left[\mathbf{P}[t-1] - \frac{\mathbf{P}[t-1] \cdot \Phi[t] \cdot \Phi^T[t] \cdot \mathbf{P}[t-1]}{\lambda + \Phi^T[t] \cdot \mathbf{P}[t-1] \cdot \Phi[t]} \right]}{\lambda} \quad (7)$$

Bayesian GPMs

A Gaussian Process Models (GPM) is a powerful tool within the field of probabilistic machine learning techniques that finds applications in many fields,^{71–74} including vibration-based SHM.^{56–59,62} For a comprehensive treatment of GPMs, the readers are directed to the book by Rasmussen and Williams.⁷⁵ The following is an outline of how GPRMs work.

Formulation. Given a training data set \mathcal{D} containing n inputs-observation pairs $\{\mathbf{x}_i \in \mathbb{R}^D, y_i \in \mathbb{R}, i=1, 2, 3, \dots, n\}$, a standard (homoscedastic) GPRM can be formulated as follows:

$$y = f(\mathbf{x}) + \epsilon \quad (8)$$

where, in a Bayesian setting, a GP prior with mean $m(\mathbf{x})$ and covariance $k(\mathbf{x}, \mathbf{x}')$ is placed on the latent function $f(\mathbf{x})$, and an independent, identically-distributed (*iid*), zero-mean Gaussian prior with variance σ_n^2 is placed on the noise term ϵ , that is:

$$f(\mathbf{x}) \sim \mathcal{GP}(m(\mathbf{x}), k(\mathbf{x}, \mathbf{x}')), \quad \epsilon \sim iid \mathcal{N}(0, \sigma_n^2) \quad (9)$$

As is common in the GPRM literature, $m(\mathbf{x})$ is set to zero, and the squared exponential covariance function (kernel) is used for the latent function GP, owing to its ability to monotonically decrease as input values go farther from each other (using a “length scale” hyperparameter), which allows for similar latent function values for close input points, and vice versa:

$$k(\mathbf{x}, \mathbf{x}') = \sigma_0^2 \exp\left(-\frac{1}{2}(\mathbf{x} - \mathbf{x}')^T \Lambda^{-1} (\mathbf{x} - \mathbf{x}')\right) \quad (10)$$

In Equation (10), σ_0^2 is the output variance, and Λ^{-1} is the inverse of a diagonal matrix of the characteristic input length scales corresponding to each dimension (D , i.e., each covariate) in the input data. For a single-input dimension (i.e., $D=1$), the entries along the diagonal of Λ^{-1} will be identical; otherwise, there will be a separate input length scale for every covariate in the training input data.

Training. Training of the GPRM involves optimizing the hyperparameters ($\boldsymbol{\theta} \equiv \sigma_0^2, \Lambda, \sigma_n^2$), which is typically done via type II maximum likelihood (chapter 5, p. 109),⁷⁵ whereas the marginal likelihood (evidence) of the training observations is maximized (or its negative

log is minimized for reasons related to computational stability). That is, the following expression is minimized with respect to Θ :

$$-\log p(\mathbf{y}|X, \Theta) = -\log \mathcal{N}(\mathbf{y}|\mathbf{0}, K_{XX} + \sigma_n^2 \mathbb{I}) \quad (11)$$

$$= -\frac{1}{2} \mathbf{y}^T (K_{XX} + \sigma_n^2 \mathbb{I})^{-1} \mathbf{y} - \frac{1}{2} \log |K_{XX} + \sigma_n^2 \mathbb{I}| - \frac{n}{2} \log 2\pi \quad (12)$$

In the expression above, K_{AB} denotes $K(A, B)$ (covariance matrix), \mathbb{I} the identity matrix, and X is the training input matrix, with the elements of each row ($\mathbf{x}_i \in \mathbb{R}^D$) carrying the different input covariates (with dimension D), and the number of rows ($i = 1, 2, 3, \dots, n$) indicating the number of input samples.

Prediction. Prediction can be done by assuming joint Gaussian distribution between the training observations (\mathbf{y}), and a test observation (y_* —to be predicted) at the set of test inputs (\mathbf{x}_*) as follows:

$$\begin{bmatrix} \mathbf{y} \\ y_* \end{bmatrix} = \mathcal{N} \begin{bmatrix} \mathbf{0}, & K_{XX} + \sigma_n^2 \mathbb{I} & \mathbf{k}_{X\mathbf{x}_*} \\ \mathbf{k}_{\mathbf{x}_* X} & k_{\mathbf{x}_*\mathbf{x}_*} + \sigma_n^2 \mathbb{I} \end{bmatrix} \quad (13)$$

where $\mathbf{k}_{X\mathbf{x}_*}$ is the vector of covariances between X and \mathbf{x}_* . By invoking the properties of multivariate Gaussian distributions,⁷⁶ the predictive distribution over y_* can be defined as follows:

$$p(y_*|\mathbf{x}_*, X, \mathbf{y}) = \mathcal{N}(\mathbb{E}\{y_*\}, \mathbb{V}\{y_*\}) \quad (14)$$

$$\mathbb{E}\{y_*\} = \mathbf{k}_{\mathbf{x}_* X} (K_{XX} + \sigma_n^2 \mathbb{I})^{-1} \mathbf{k}_{X\mathbf{x}_*} \quad (15)$$

$$\mathbb{V}\{y_*\} = k_{\mathbf{x}_*\mathbf{x}_*} - \mathbf{k}_{\mathbf{x}_* X} (K_{XX} + \sigma_n^2 \mathbb{I})^{-1} \mathbf{k}_{X\mathbf{x}_*} + \sigma_n^2 \quad (16)$$

such that $\mathbb{E}\{y_*\}$ and $\mathbb{V}\{y_*\}$ are the predictive mean and variance, respectively, at the set of test inputs.

TAR parameter-based GPRMs

Figure 2 shows the overall flow of the methodology presented in this paper for damage and/or loading state estimation. In this work, each TAR model parameter (see Figure 1 for an example of a TAR parameter) is used in training GPRMs across the different input states (damage size alone or both damage size and loading state). Thus, in this case, for a four-parameter TAR model, four GPRMs are trained and used for prediction. As mentioned in section “Time-varying autoregressive models,” one of the most important features of using TAR model parameters in training quantification models is the ability to freely select the time instant at which to quantify damage. This allows for flexibility in exploring the different parts of a guided-wave response signal, searching for damage sensitive features that can potentially lead to more accurate

damage quantification results. In addition, unlike DI-based GPRMs⁶⁷ or those based on non-parametric time series models,⁶⁶ TAR-based GPMs do not face the drawback of having to select specific reference signals when doing the prediction. This again makes the use of TAR model parameters in training GP quantification models very appealing. This being said, the task of training GPRMs with single/multiple TAR parameters identified for each damage and/or load states, at each time instant, and with many realizations is far from trivial. The amount of available data makes it inefficient to train regular GPRMs even when using active learning algorithms (since a huge amount of training data will still be required to train capable GPRMs). Thus, a single-time instant framework was developed in order to tackle this problem whilst getting the best out of the available time-based information. The following subsection present briefly the framework used in this work to select the time points at which to train GPRMs.

Selection of time instants. As mentioned above, due to the amount of data points needed for training GPRMs under multiple damage and load states as well as multiple time instants and cross-sections, a time-instant selection framework was developed in order to train GPRMs only at those time instants in the signals where there is a significant change in amplitude with damage and/or loading states. The most “sensitive” time instants were selected based on the difference between the TAR parameter values at each damage state and those at the healthy state. With the availability of multiple realizations of signals, the mean of the corresponding realizations of the studied parameter was used in calculating the difference. Furthermore, the difference was also normalized by the standard deviation of the multiple realizations of the selected parameter in the healthy case ($\sigma_{\alpha_{n,H}(t)}$). Thus, the metric based on which the time instants were chosen was formulated as follows for each loading state:

$$(\mathbb{E}\{\alpha_{n,H}(t)\} - \mathbb{E}\{\alpha_{n,D_i}(t)\}) / \sigma_{\alpha_{n,H}(t)} \quad (17)$$

This normalized difference is calculated for each damage state, then each load, then each parameter. After that, these vectors are sorted, and the time instants that give out the largest differences across all damage states, loads, and parameters are selected for training the GPRMs. Figure 3 shows a schematic of this time-instant selection technique for the single-parameter framework presented herein. Figure 1(b) shows an example of the parameter differences shown in Equation (17) applied to parameters from the unloaded state of the coupon before sorting with respect to the largest difference. It is worth emphasizing here that the

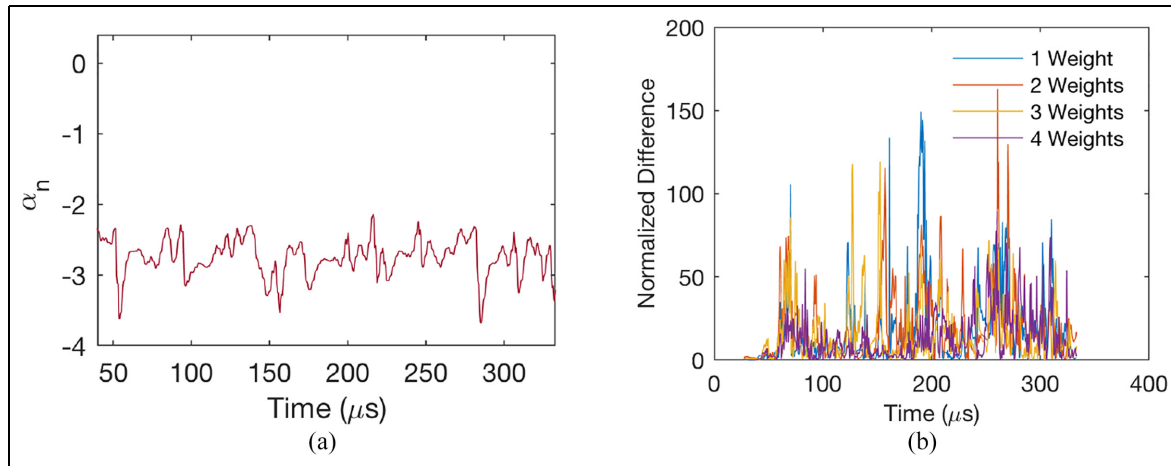


Figure 1. (a) An example of the evolution of a TAR parameter with time. (b) An example of the normalized difference calculated for one TAR parameter for all damage cases at the no-loading condition.

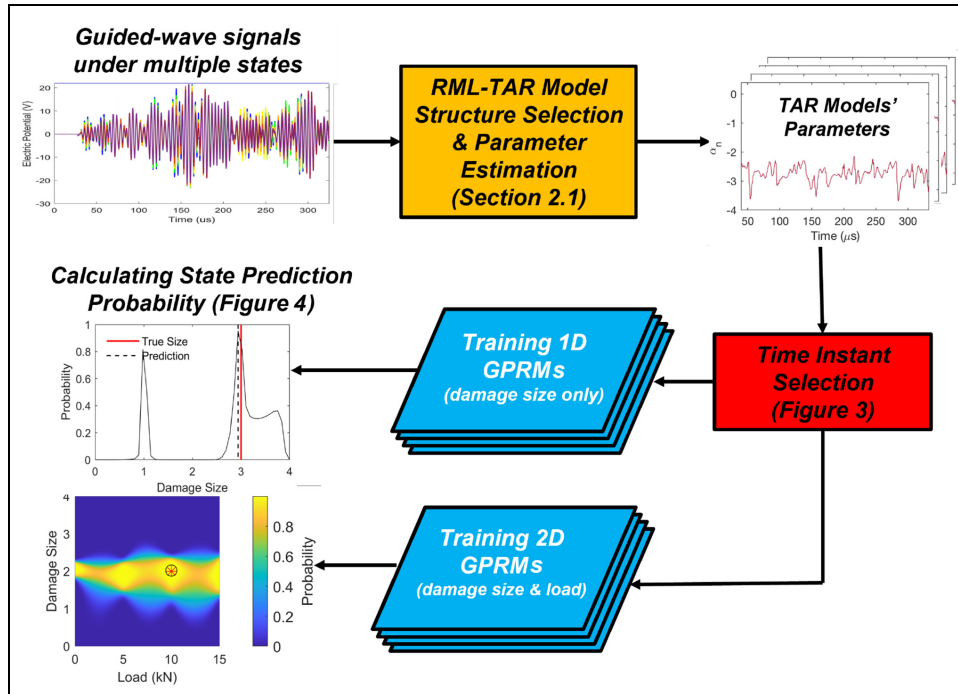


Figure 2. A high-level summary of the methodology presented in this work for damage and/or load state(s) estimation.

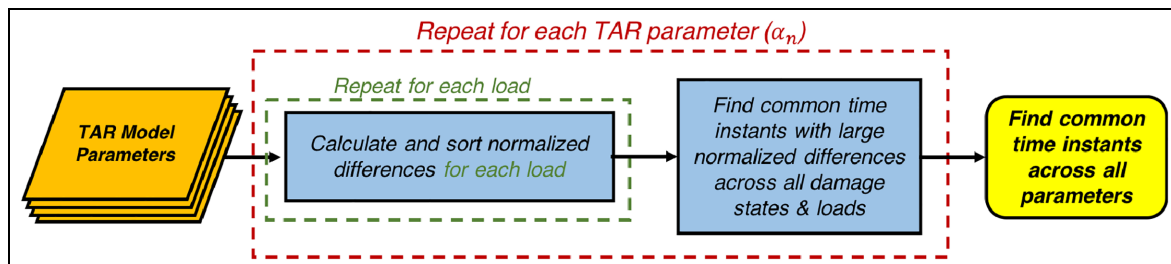


Figure 3. A schematic flow chart showing the proposed framework for selecting time instants at which to train TAR-based GPRMs. GPRM: Gaussian Process regression model.

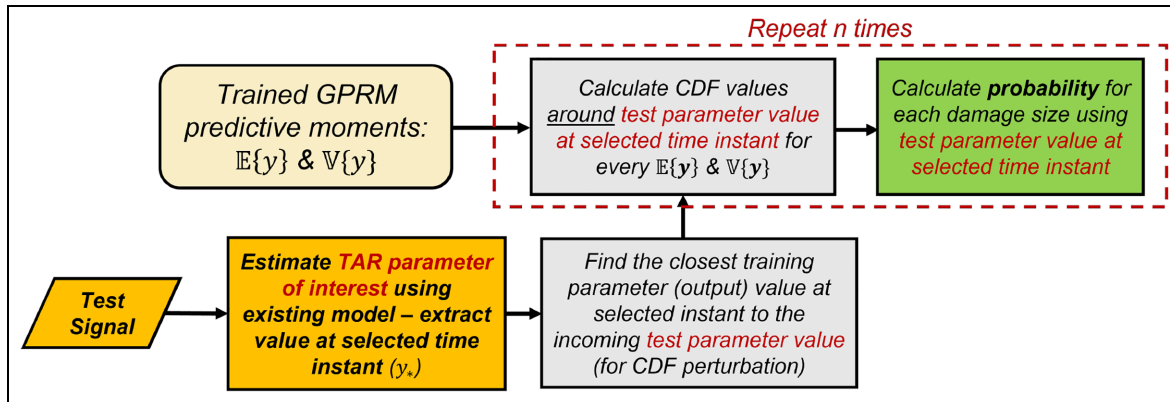


Figure 4. A schematic flow diagram showing the steps taken in this study to calculate the state prediction probability.

selection technique is applied across all loads and all parameters before selecting the proper time instants. Also, because it is not always the case that this selection process would converge to a single time instant across all damage sizes, loads, and parameters, multiple large-difference time instants can be selected at this stage for training multiple single-parameter GPRMs.

With the framework for selecting the time instants outlined, a few remarks need to be discussed before moving on with presenting the results. Firstly, looking at Equation (17), one can argue that comparing the parameter values at each damage state with these at the healthy state would allow for selecting time instants that favor the process of damage detection, not quantification. This is because the time instants are selected based on the deviation of each damage state from the healthy state, not the deviation of each damage state from other damage states. This might lead to selecting time instants at which the parameter values for all damages are quite distinctive from those at the healthy state, but not distinctive from each other, throwing off quantification efforts. Although this is plausible, the reason why this approach was still pursued for time-instant selection in this work is because of the lack of overlap between the time instants that make all damage states distinctive from the healthy state and at the same time distinctive from each other.

Another point worth mentioning is that, in Equation (17), the difference of parameter values is considered across damage sizes and not loading states, which might favor damage size quantification at the expense of load quantification. Although the selected time instants are then analyzed across all loading states in a later step (and then across all parameters), the results would still favor damage size quantification. This phenomenon can potentially be avoided if Equation (17) is calculated across loading states then across damage states, and then the common time

instants from both analyses are selected for quantification. This approach, however, is beyond the scope of this work, which focuses mainly on introducing TAR-GPRMs as a means to more temporally educated state quantification processes.

Damage state quantification. In many practical cases, such as the case in this study, the test observations at which prediction should take place are actually the GPRM targets, not the inputs, that is, in this study, the single-time-instant, fitted TAR parameter(s) for the incoming test signal (y_* —target) would be available, and the damage size and/or load state (\mathbf{x}_* —inputs) would have to be inferred by the GPRM. In this work, the proposed method of estimating the inputs from the test target values is based on the probability that a test target value y_* belongs to a specific damage size and/or load state \mathbf{x} . Figure 4 schematically outlines the steps to calculate the state (input) prediction probability in this case. As shown, this probability ($P(\mathbf{x}_* = \mathbf{x})$) can be estimated from the cumulative distribution function (CDF) of the targets as follows:

$$P(\mathbf{x}_* = \mathbf{x}) = F_y(b; E\{y\}, V\{y\}) - F_y(a; E\{y\}, V\{y\}) \quad (18)$$

such that,

$$F_y(s; \mu, \sigma) = \frac{1}{\sigma\sqrt{2\pi}} \sum_{t=-\infty}^s e^{-\frac{(t-\mu)^2}{2\sigma^2}} \quad (19)$$

$$a = y_* - 2\sqrt{V\{y_{\text{closest}}\}} \quad (20)$$

$$b = y_* + 2\sqrt{V\{y_{\text{closest}}\}} \quad (21)$$

such that y_{closest} is the closest training parameter value (at the selected time instant—see section “Selection of time instants”) to the value of the incoming test parameter value (y_*), and $V\{y_{\text{closest}}\}$ is the predictive

variance corresponding to that point. $\mathbb{E}\{y\}$ and $\mathbb{V}\{y\}$ respectively indicate the predictive mean and variance at the training input x . Also, $F_y(\cdot)$ is the output CDF value at the enclosed point and distribution. Calculating this probability for all sets of inputs allows for identifying the set of states with the highest probability (the GPRM prediction in this case). It is worth noting here that the uncertainty in the model, as defined by the GPRM predictive variance, corresponding to the training TAR parameter value closest to the incoming test one is used here in order to properly estimate the probability of damage size and/or load state.

Experimental setup

An Al coupon of dimensions $152.4 \times 279.4\text{mm}$ ($6 \times 11\text{in}$), $2.36\text{mm}/0.093$ in thickness, was used in this study. Six lead zirconate titanate (PZT) piezoelectric sensors (type PZT-5A from Acellent Technologies, Inc, Sunnyvale, California, USA), with diameter 3.175 mm ($1/8\text{in}$) and thickness 0.2 mm (0.0079in), were attached to the coupon using Hysol EA 9394 adhesive (Henkel North American Consumer Goods, Rocky Hill, Connecticut, USA). After that, the adhesive was left under vacuum for curing in room temperature for 24 h. The coupon was then mounted on a tensile testing machine (Instron, Inc, Norwood, MA, USA), and five static loading experiments were run consecutively (0, 5, 10, and 15 kN). During each loading experiment, up to 4 three-gram weights, each around 6 mm 6 mm in diameter and 1 cm (0.39in) in height, were attached to the coupon's surface using tacky tape, starting from the center of the coupon, and moving toward the right on the side where the sensors were attached as shown in Figure 5. It is important to note here that this type of damage simulator was selected only to showcase the applicability and effectiveness of proposed framework, and although attached weights have been used in the SHM literature as a standard method of simulating some types of damage (see for instance, the study by Moll et al.⁷⁷ for guided-waves and the study by Kopsaftopoulos and Fassois⁷⁸ for vibration-based SHM), a more realistic form of damage should be used for validating the proposed framework in the future (such as the one presented in the study by Yue and Aliabadi⁷⁹).

Having an amplitude of 90 V peak-to-peak and various center frequencies, 5-peak tone bursts (five-cycle Hamming-filtered sine waves) were generated as actuation signals at each sensor. Using a pitch-catch paradigm, signals received at the sensors across the coupon from the sensor being actuated in each experiment were collected using a ScanGenie III data acquisition system (Acellent Technologies, Inc). Repeated 20 times

for each actuator, 20 signals per sensor per damage per loading conditions (2400 signal sets) were acquired in total. A center frequency of 250 kHz was chosen for the damage quantification based on the best separation between the two first-arrival wave packets in various actuator-sensor signals. For the analysis shown herein, sensor path 2-6 was used while results from another sensor path are shown in the Appendix. TAR model parameters were estimated for all damage and loading conditions, and GPRMs were trained using a single parameter/GPRM, in which only a specific time instant within the selected parameter across all training damage and loading states was used for training. It is important to note here that a substantial amount of data was used for GPRM training (substantial compared to the number of input dimensions—see Tables 2 and 3) in order to reduce the impact of epistemic uncertainty on the accuracy of predictions from the proposed framework, and to better allow for the assessment of the framework based on its overall performance. The normalized mean squared error and the RSS/SSS were calculated for the trained GPRMs using test data. Matlab (Matlab version R2020a, GPRM training, and prediction: the different functions within the GPML package available at <http://www.gaussianprocess.org/gpml/code/matlab/doc/index.html>) was used for post processing of the signals and training the GPRMs.

Results and discussion

The parametric identification of the wave propagation signals was achieved via TAR models based on 612 ($332\text{ }\mu\text{s}$) sample-long response signals (sampling frequency $f_s = 2\text{ MHz}$) recorded via embedded piezoelectric sensors. The model order and forgetting factor estimation, that is, the model “structure” selection problem, was based on the successive estimation of TAR(na) models for orders $na = 2, \dots, 22$ and forgetting factors $0.500, \dots, 0.999$ with an increment of 0.001. Figure 6(a) shows the model selection via the RSS/SSS criterion. Note that the model order $na = 4$ and $\lambda = 0.835$ results in the lowest RSS/SSS value (0.1267%). Figure 6(b) shows the evolution of the Bayesian Information Criterion (BIC)^{80,81} with the model order and the forgetting factor. Note that the BIC value drastically drops until $na = 8$, and after that decreases very slowly with the increase in model order. Thus, the BIC criterion would suggest the use of model order $na = 8$. However, from Figure 6(a), using model order $na = 8$ does not decrease the RSS/SSS value. Additionally, using a higher model order necessitates the estimation of the higher number of parameters, and may introduce spurious frequencies.⁸² Thus the best model was selected based on the combined consideration

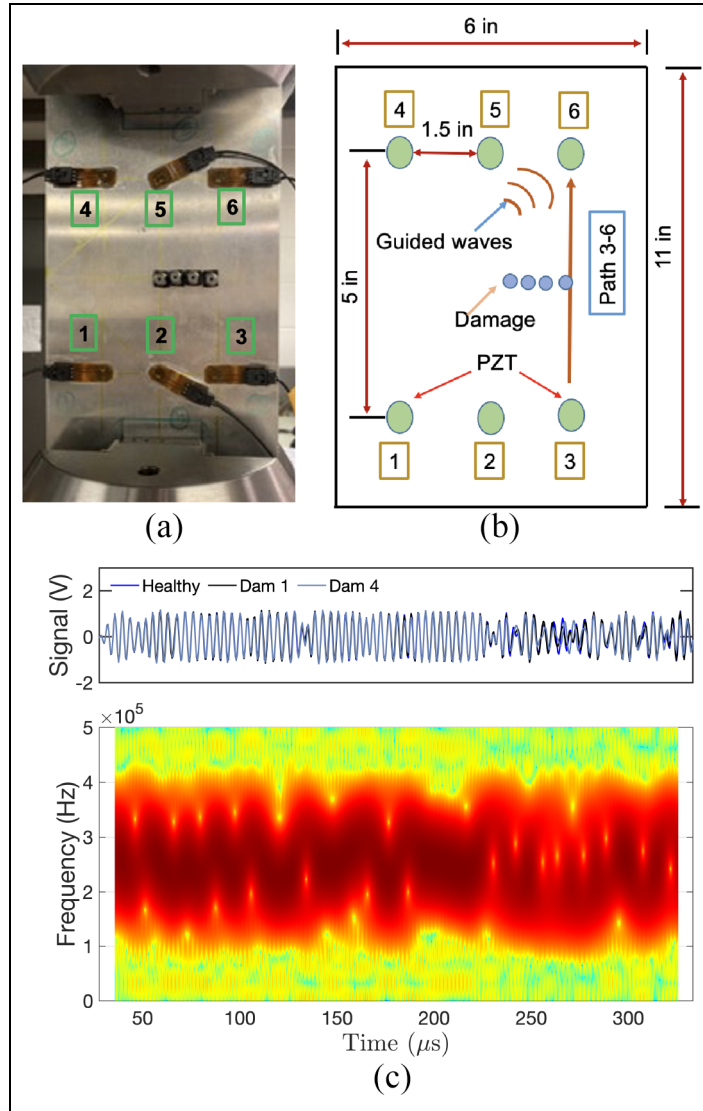


Figure 5. (a) The Al plate used in this study, (b) a schematic of the plate's sensor layout and dimensions, and (c) realization of the guided wave signal for healthy and damaged cases with a representative non-parametric spectrogram analysis.
Al: aluminum.

of the BIC,^{80,81} RSS/SSS criterion,^{44,48} and the comparison with the corresponding non-parametric spectral estimates.⁸³ This process resulted in a final model of order $na=4$ and forgetting factor 0.835, designated as RML-TAR(4)_{0.835}, for representing the non-stationary wave propagation signal.

Figure 7 shows the one-step-ahead prediction of the segment of a representative guided wave signal using the identified RML-TAR(4)_{0.835} model. Note that at the beginning, the prediction error is higher (due to limited available data), however, as more and more data become available (recursive estimation), the prediction error goes close to zero and the percent RSS/SSS value is 0.1267%. This indicates that the

non-stationary guided wave signal was modeled with high accuracy.

Figure 8 shows the evolution of the four estimated parameters of the RML-TAR(4)_{0.835} model with damage size at the no-loading condition in path 2–6 in the Al coupon (see Figure 5 for sensor numbering). Figure 9 shows the zoomed-in view of Figure 8. The ± 3 standard deviations confidence intervals of the healthy parameters are also shown. The fluctuation in the parameters originates from them adapting to the signals being modeled at every time instant due to the nature of the recursive algorithm. Also, as shown, the effect of damage on the parameters is not uniform across the different time instants since the parameters "mimic"

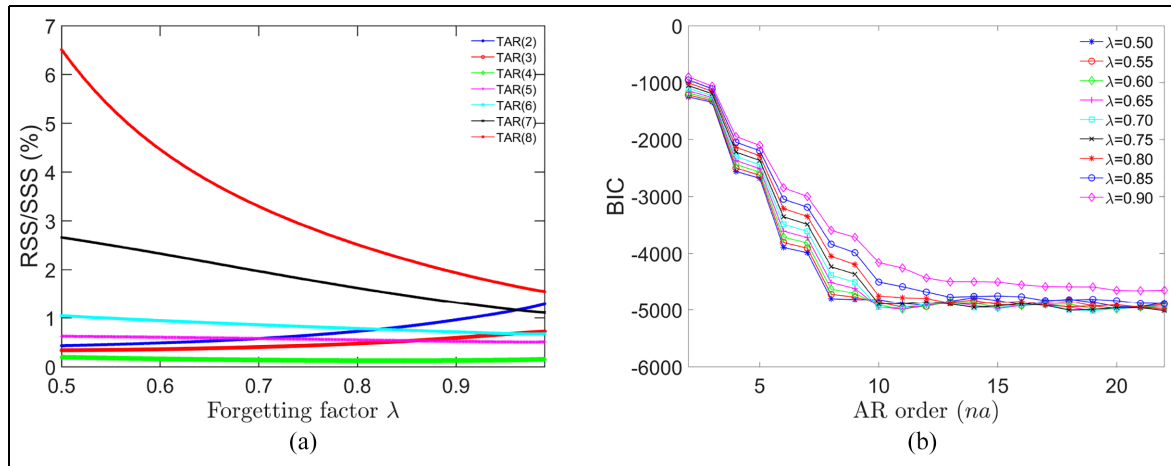


Figure 6. RML-TAR model order selection for one-step-ahead prediction of a representative guided wave signal: (a) shows the change in percent RSS/SSS values versus the forgetting factor and (b) shows the reduction of the BIC values over increasing model orders.

RML: recursive maximum likelihood; BIC: Bayesian Information Criterion; SSS: signal sum of squares; RSS: residual sum of squares.

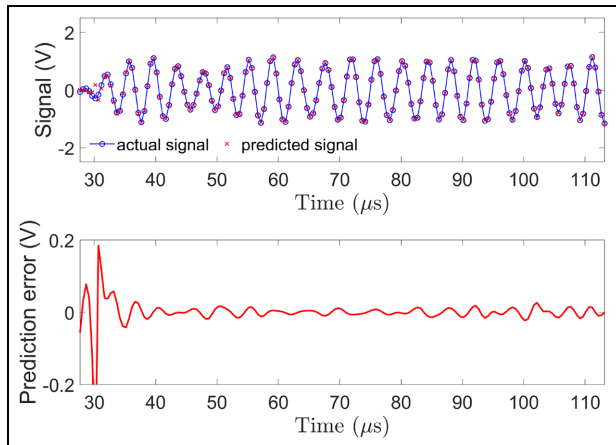


Figure 7. Segment of a non-stationary guided wave signal realization (S_0, A_0 mode and part of the reflected signal) superimposed with RML-TAR based one-step-ahead prediction and the corresponding residual obtained by RML-TAR(4)_{0.835}. RML: recursive maximum likelihood.

the true signals, which also exhibit the same phenomenon. Finally, it can also be observed that the effect of damage is relatively small across the first 150 μ s compared to later on the time axis, which shows the importance of the time-instant selection algorithm mentioned above, for which results are presented in the following section. Figure 10 shows the corresponding plots for the case of a 10-kN applied load. Figure 11 shows the zoomed-in view of Figure 10. Note the similarity in parameter evolution with time between the 0-kN and the 10-kN cases again up to about 150 μ s, which is followed by a region of deviation between the parameters across both loading cases. These parameters were then

used in training single-parameter GPRMs (one GPRM per parameter) either at a specific load (single-input GPRMs) or at all loads at once (multi-input GPRMs).

Time-instant selection results

Following the estimation of the model parameters, the time-instant selection algorithm, as described in section “Selection of time instants,” was applied. Table 1 presents the first 10 time instants selected by the selection strategy described above. It is important to note here that the selected time instants shown in Table 1 were compiled from the commonly selected time instants across at least three out of four parameters at every damage and load state. As shown in Table 1, all of the selected time instants based on the individual parameters lie beyond 150 μ s, which can be understood given the observations outlined above with the parameter evolution after that time instant. In this study, two time instants (highlighted in blue in Table 1) were selected for damage and/or damage and load state quantification. These two time instants (177.7 and 188.2 μ s) were selected in particular since these are amongst the top time instants across all 4 parameters. The results from the first time instant are shown in the main body of this work, while the results from the latter instant (amongst others) are shown in the Appendix.

Damage size quantification results

As described above, single-parameter GPRMs were trained using TAR parameter data at 177.6667 μ s at each loading state (one GPRM for each load value) in

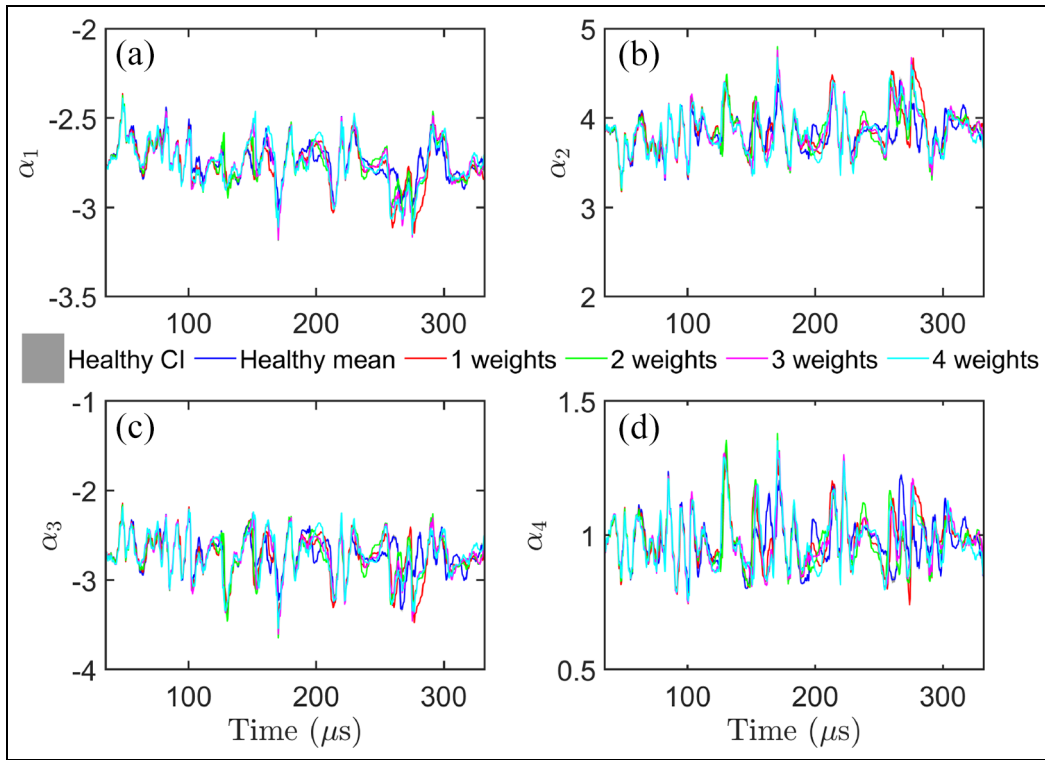


Figure 8. The evolution of indicative RML-TAR(4)_{0.835} model parameters with damage size (added weights) at a loading state of 0 kN for path 2–6: (a) $\alpha_1(t)$, (b) $\alpha_2(t)$, (c) $\alpha_3(t)$, and (d) $\alpha_4(t)$. The ± 3 standard deviations confidence intervals of the healthy parameters are also shown.
RML: recursive maximum likelihood.

Table I. The first 10 time instants*(μs) selected by the strategy described in section “Selection of time instants” for path 2–6 of the Al coupon.

175.7	177.2	177.7	188.2	188.7	189.2	189.7	190.2	190.7	191.2
-------	-------	-------	-------	-------	-------	-------	-------	-------	-------

Al: aluminum.

The blue color highlights the time instants for which the quantification results are presented herein.

*Time instants approximated to the first decimal place.

Please refer to the online version of the article to view the text colour described in this table.

order to assess the damage quantification performance of TAR-GPRMs when the load is known. Table 2 presents summary model information for the trained GPRMs. Figures 12 and 13 show the predictive means and confidence bounds from eight trained GPRMs for the first and the fourth parameter (four GPRMs each), respectively, under different loading states. The first and fourth parameters were chosen here since they show different evolutions with time, and because the other two parameters show similar behaviors as shown in Figures 8 and 10. Looking at Figures 12 and 13, one can see that the trained GPRMs follow the evolution of the parameters to a good degree of accuracy with slight over-fitting in some inter-damage size regions. Also, the evolution of

the parameters with damage size seems to be uniform to some extent, with some saturation occurring around the one- and two-weight cases (Figure 12(b) and (c) and Figure 13(c)) or the three- and four-weight cases (Figure 12(b) and all loading states in Figure 13). This saturation would generally lead to poor quantification accuracy in its vicinity. Looking closer at both figures, it can be observed that saturation around the two-weight case occurs only when the coupon is exhibiting a non-zero load. This phenomenon sheds some light on the nature of the effect of loading on this coupon. All in all, as shown in both figures, the remaining damage states exhibit good separation with respect to the parameter values, which indicates the effectiveness of the time-instant selection

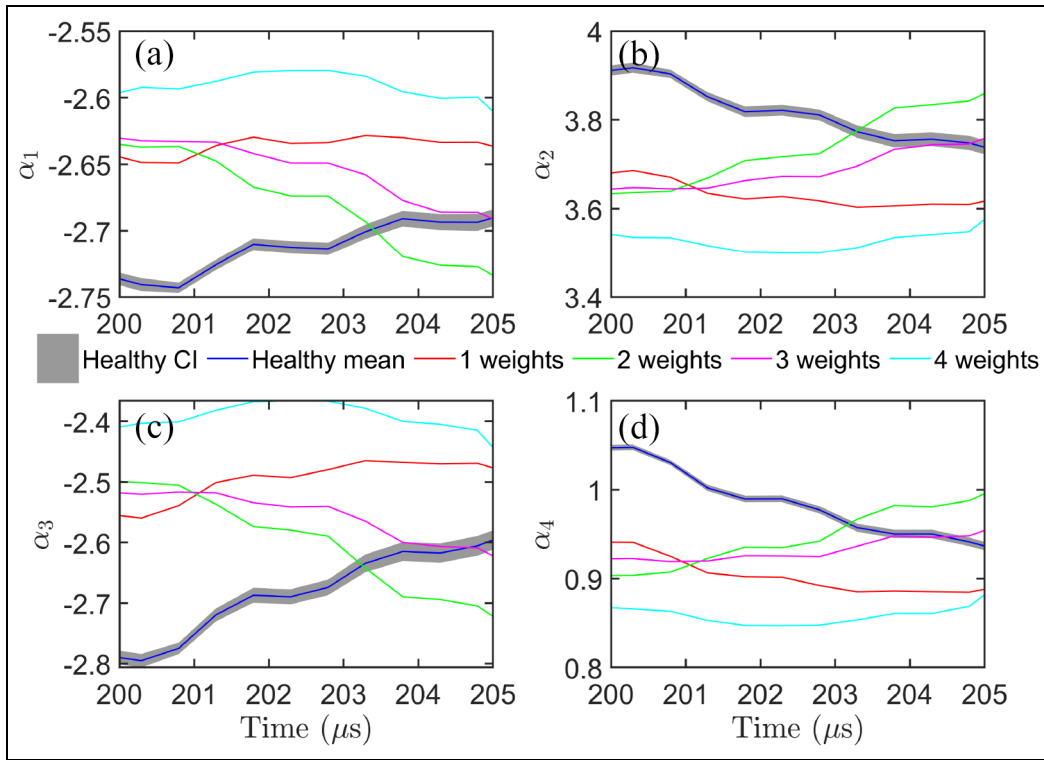


Figure 9. The zoomed-in view of the evolution of part of the indicative RML-TAR(4)_{0.835} model parameters with damage size (added weights) at a loading state of 0 kN for path 2–6: (a) $\alpha_1(t)$, (b) $\alpha_2(t)$, (c) $\alpha_3(t)$, and (d) $\alpha_4(t)$. The ± 3 standard deviations confidence intervals of the healthy parameters are also shown.
RML: recursive maximum likelihood.

Table 2. Summary of single-input TAR-GPRM* information[†] for path 2–6 in the Al coupon with simulated damage at each loading state 177.6667 μ s.

Parameter	NMSE				RSS/SSS (%)			
	0 kN	5 kN	10 kN	15 kN	0 kN	5 kN	10 kN	15 kN
α_1	5.34E-4	4.24E-4	1.10E-3	9.05E-4	1.65E-6	1.87E-6	3.38E-6	2.487E-6
α_2	4.84E-4	2.62E-4	8.90E-4	5.90E-4	2.71E-6	2.05E-6	5.91E-6	3.72E-6
α_3	5.54E-4	3.54E-4	6.54E-4	6.56E-4	5.57E-6	5.00E-6	7.77E-6	7.76E-6
α_4	2.10E-3	8.33E-4	8.97E-4	7.10E-4	1.78E-5	9.44E-6	9.18E-6	8.62E-6

Al: aluminum; NMSE: normalized mean squared error; SSS: signal sum of squares; RSS: residual sum of squares.

*Twenty-five percent (50 points) of the data was used for training each model.

[†]Numbers approximated to the last quoted decimal place,

process outlined above in identifying instants at which the signals show significant deviations with increasing damage size.

Figure 14 shows the prediction summary results for the first parameter at 177.6667 μ s under each loading state. The first observation that can be drawn from these results is that the overall damage size quantification performance of this parameter is very good. Secondly, it can be seen that although the effects of saturation around specific damage sizes did propagate

to the quantification results as shown in panels (a) and (b) around the three- and four-weight cases, in some cases, the model was still capable of identifying the correct damage size prediction medians as outlined by the horizontal red lines in the boxes in panel (c) around the single-weight case and in panel (d) around the four-weight case. Moving onto the summary results from the fourth parameter (Figure 15), similar observations can be made, noting a slightly more-pronounced effect of parameter saturation around the last two

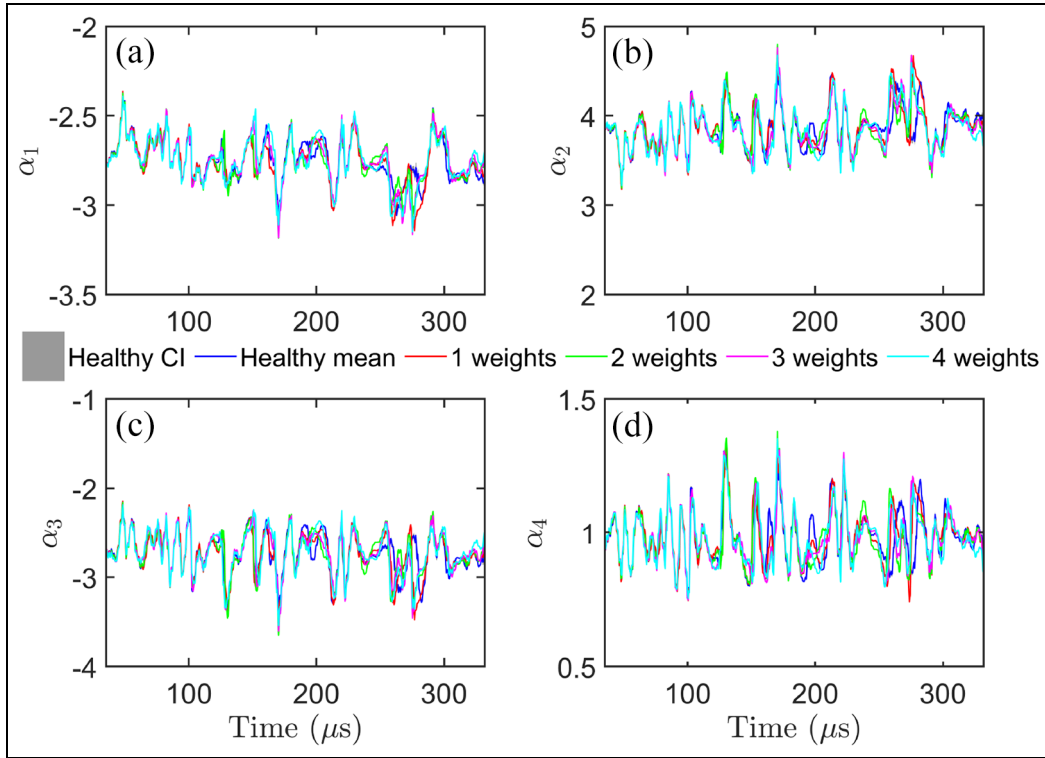


Figure 10. The evolution of indicative RML-TAR(4)_{0.835} model parameters with damage size (added weights) at a loading state of 10 kN for path 2–6: (a) $\alpha_1(t)$, (b) $\alpha_2(t)$, (c) $\alpha_3(t)$, and (d) $\alpha_4(t)$. The ± 3 standard deviations confidence intervals of the healthy parameters are also shown.
RML: recursive maximum likelihood.

damage states. It is important to note here that results from the second and third parameters were similar (not shown here), hinting at the overall effectiveness of this single-parameter approach, and its critical dependence on the selected time instant.

Simultaneous damage size and load quantification results

Because of the case in many real-world scenarios, it is of interest to present some indicative state quantification results where both damage size and load are unknown. Thus, multi-input GPRMs were trained using single-parameter data across all damage sizes and loading states (only one model for each parameter) for which summary model information is presented in Table 3. Note that training and prediction times were very small and are thus not quoted in this table. Presenting the first indicative results from single-parameter models, Figure 16 shows the two-dimensional predictive means and standard deviations for the model trained using the first parameter data (panels (a) and (b)) and the fourth parameter data (panels (c) and (d)). Looking at the standard deviations of the GPRMs of both parameters (panels

Table 3. Summary of multi-input TAR-GPRM* information[†] for path 2–6 in the Al coupon with simulated damage at 177.2 μ s.

Parameter	NMSE	RSS/SSS
α_1	1.60E-3	1.35E-4
α_2	5.99E-4	4.01E-6
α_3	5.10E-4	6.38E-6
α_4	8.63E-4	1.01E-5

Al: aluminum; SSS: signal sum of squares; RSS: residual sum of squares; NMSE: normalized mean squared error.

*Fifty percent (200 points) of the data was used for training each model.

[†]Numbers approximated to the last quoted decimal place.

(b) and (d)), one can observe the somewhat periodic behavior of the predictive confidence bounds from one damage state to another, which indicates the increasing uncertainty between training data points. With respect to loading states, this phenomenon does exist only slightly as can be seen in the dark blue regions in the panels. The reason why the periodicity in the predictive confidence bounds is less significant with load than with damage size is attributed to the optimized hyperparameters with respect to each input, which might originate

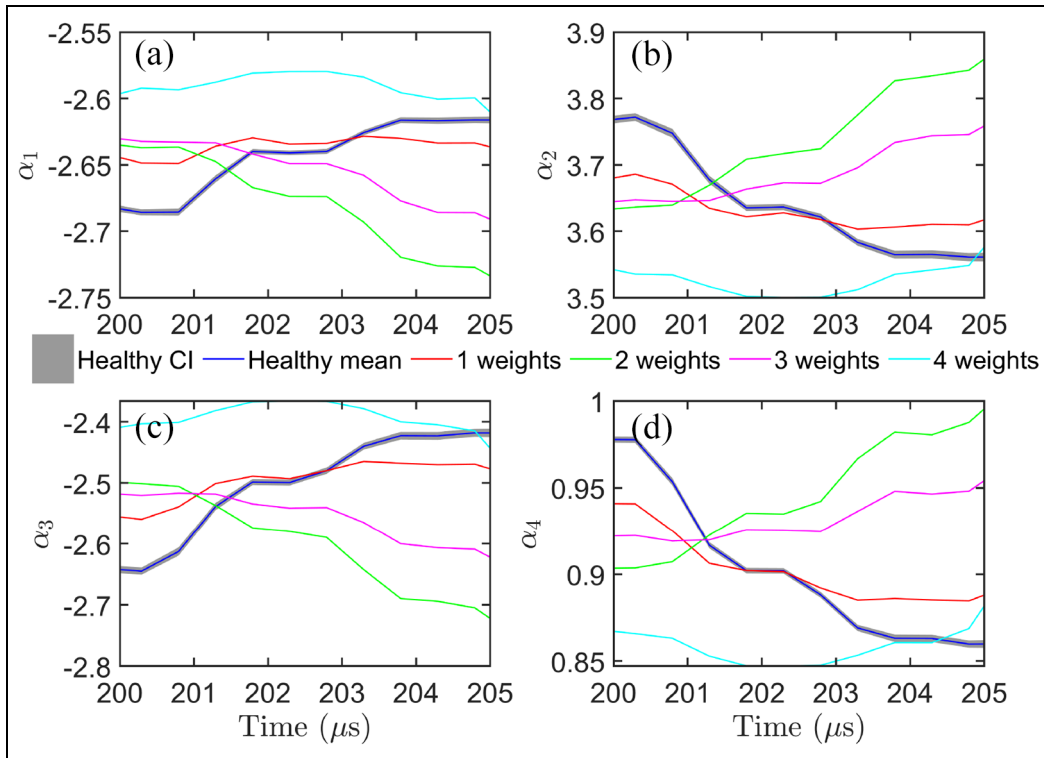


Figure 11. The zoomed-in view of the evolution of part of the indicative RML-TAR(4)_{0.835} model parameters with damage size (added weights) at a loading state of 10 kN for path 2–6: (a) $\alpha_1(t)$, (b) $\alpha_2(t)$, (c) $\alpha_3(t)$, and (d) $\alpha_4(t)$. The ± 3 standard deviations confidence intervals of the healthy parameters are also shown.
RML: recursive maximum likelihood.

from phenomena such as the dispersion of the training data points around specific loads or damage sizes.

In order to examine more closely the evolution of the multi-input GPRMs with damage size and loading state, predictive information was extracted from each of the two multi-input GPRMs at specific loads and damage sizes. Figure 17(a)–(d) show some indicative plots presenting the evolution of the parameters with damage size at specific loading state and vice versa, and showing how the trained multi-input GPRM can accurately follow the evolution of the parameters with both inputs at the same time. As shown in panels (b) and (d), the predictive confidence bounds coming from the evolution of the first parameter with load at specific damage sizes show a uniform evolution without significant periodicity around training points, which seems to be originating from the dispersion (noise) of the training data points. For the evolution of the GPRM with damage size at specific loading states, one can notice the periodicity around the training data points, which might be originating from the low variance in the training data points at each damage size. Figure 17(e) and (f) show the two-dimensional prediction probability plots for two indicative test parameter values (not used

in training) for the cases shown collectively in panels (a) and (b), as well as panels (c) and (d), respectively. As shown, the trained GPRM can accurately identify the correct damage size and loading state in both cases. Figure 18 shows the corresponding plots from the multi-input GPRM trained using the fourth TAR parameter. Again, the same periodicity phenomenon, or lack thereof, can be seen in panels (a) and (c) or (b) and (d), respectively. Also similarly, the trained model accurately follows the evolution of the fourth parameter with damage size and load, as well as accurately predicts the correct set of states for the indicative testing points shown in panels (e) and (f).

In order to fully assess the performance of the trained TAR-GPRMs at 177.7 μ s using the single-parameter approach, prediction error results with respect to damage size and loading state were plotted as shown in Figure 19. Examining the summary results, it can be clearly observed that the trained models from both parameters are more accurate in damage size quantification compared to loading state quantification. This can be directly attributed to the selected time instant, which follows from a process that favors damage size as aforementioned in section “Selection of time instants.” As

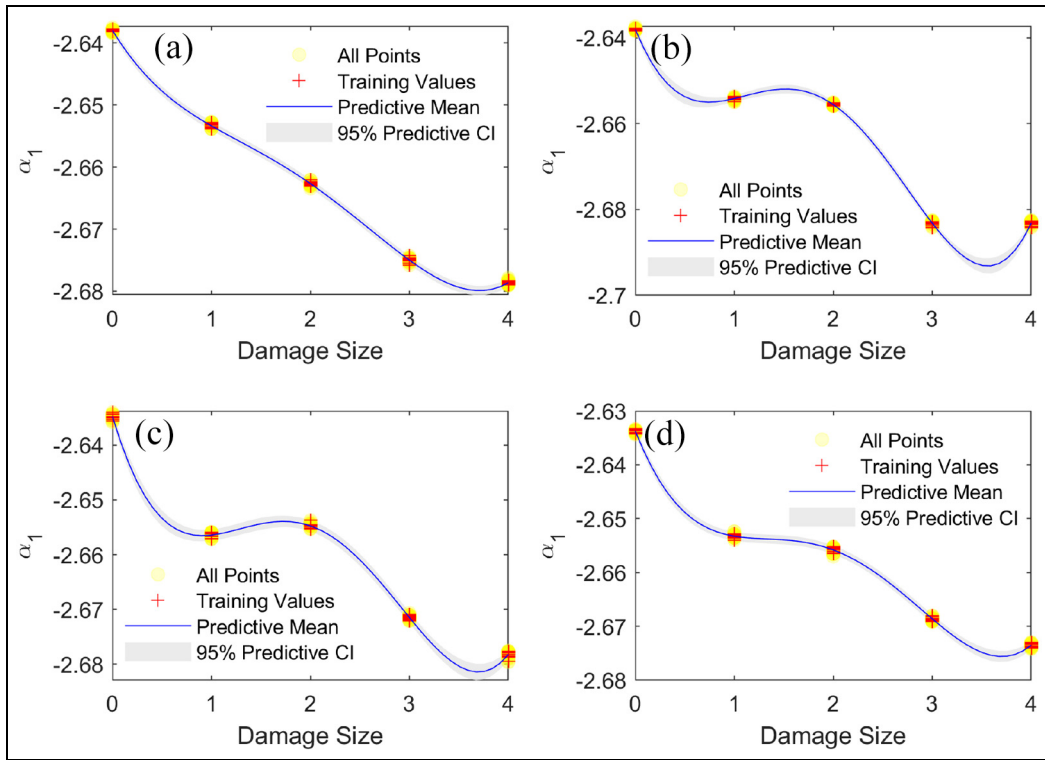


Figure 12. GPRM predictive means and confidence bounds for the first parameter at $177.7 \mu\text{s}$ with damage size under multiple loading states for path 2–6: (a) the no-loading condition, (b) the 5-kN case, (c) the 10-kN case, and (d) the 15-kN case. GPRM: Gaussian Process regression model.

also outlined therein, this phenomenon can be avoided if a more rigorous time-instant selection process is followed in which the differences between parameter values at different loading states is also considered, aside from the differences across damage sizes, then the common time instants are selected accordingly. This being said, looking at Figure 19(a) and (b), it can be deduced that the trained model struggles to accurately predict loading state at the one- and four-weight damage cases, respectively. It is also evident that the loads with which the model struggles the most are the no-loading condition as well as the 15-kN case. Similar observations can be extracted from the fourth parameter GPRM results in panels (c) and (d). In order to put these results into context, it is worth mentioning that, although the presented results here from TAR-GPRMs do not show load predictions as accurate as those from DI-trained GPRMs (see the studies by Amer et al.^{25,67} for results presented for the same coupon), the TAR-GPRM framework proposed here still shows much more flexibility as well as rigorously. The flexibility originates from the maintainers being able to simply look at the signals and freely select time instants at which to do state predictions, which is a feature only entertained by TAR-GPRMs. The rigorously comes from the TAR models

capturing the non-stationarity within the guided-wave signals, which makes the models much more capable of describing the state of the system if their full potential is tapped into. In addition, as outlined above, the load prediction accuracy results can be enhanced by adding an extra step in the time-instant selection process. This latter remedy, however, is left as future work.

Conclusion

In this study, TAR models were identified for guided-wave time series coming from an Al plate with simulated damage under multiple loading states in order to capture the non-stationary nature of guided-wave signals. Then, the TAR model parameters were used to train GPRMs for probabilistic damage and/or loading state quantification. Applying these TAR-GPRMs, a method was devised in order to select the “most sensitive” time instants at which to tackle the state quantification problem in order to give the maintainer more flexibility in selecting the time instants in the signals that are more interesting (i.e., relevant to where damage is on the spatiotemporal space). To showcase one way of building TAR-GPRMs, one parameter was used to train single-input or multi-input GPRMs, and

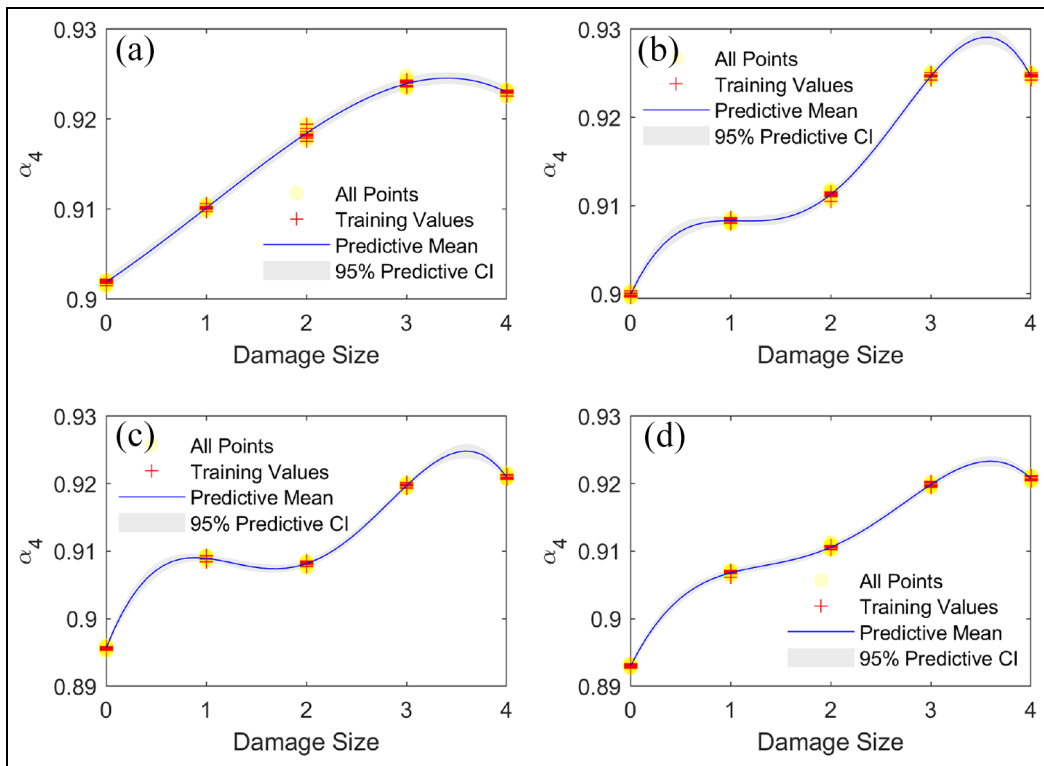


Figure 13. GPRM predictive means and confidence bounds for the fourth parameter at $177.7 \mu s$ with damage size under multiple loading states for path 2–6: (a) the no-loading condition, (b) the 5-kN case, (c) the 10-kN case, and (d) the 15-kN case.
GPRM: Gaussian Process regression model.

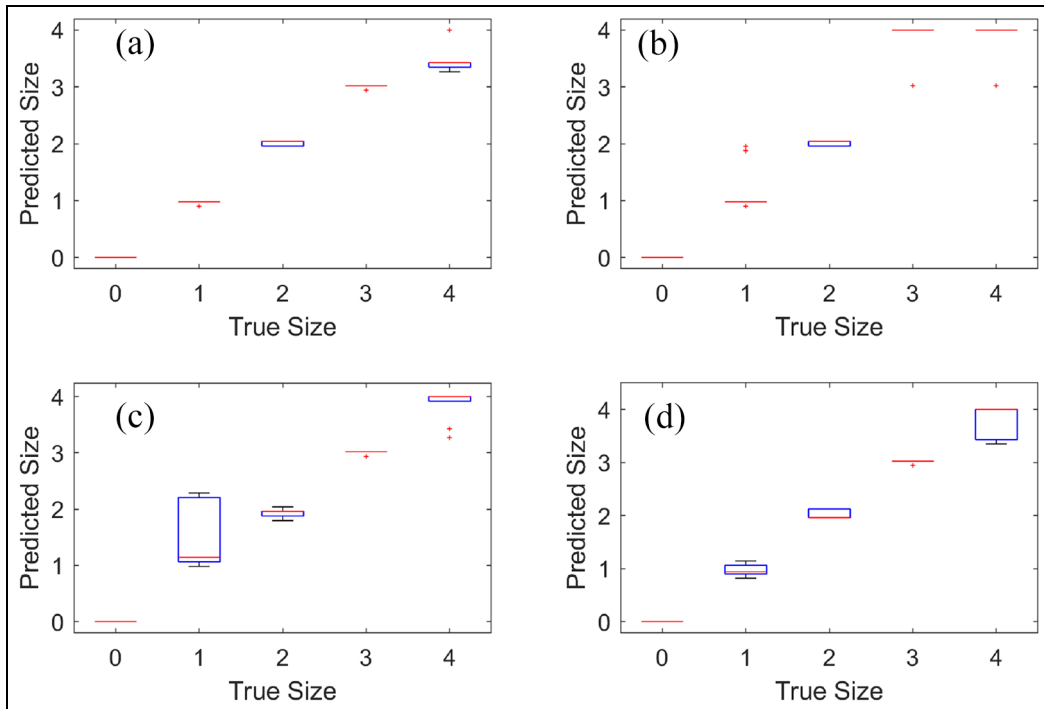


Figure 14. Prediction error boxplots for the first parameter at $177.6667 \mu s$ with damage size under multiple loading states for path 2–6: (a) the no-loading condition, (b) the 5-kN case, (c) the 10-kN case, and (d) the 15-kN case.

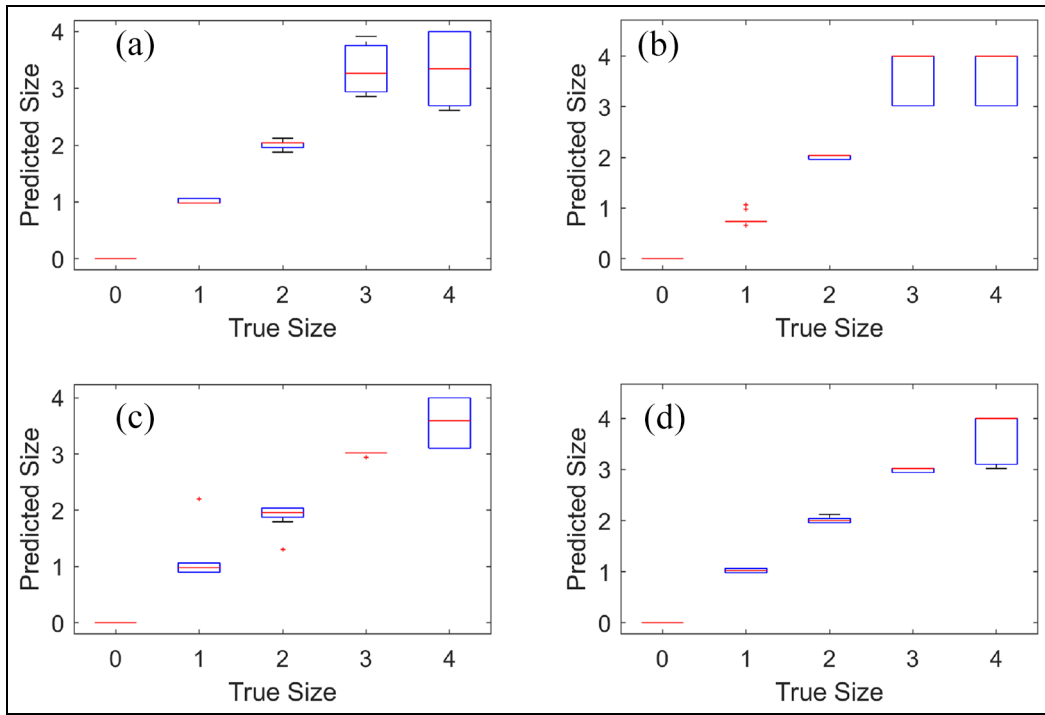


Figure 15. Prediction error boxplots for the fourth parameter at $177.7 \mu\text{s}$ with damage size under multiple loading states for path 2–6: (a) the no-loading condition, (b) the 5-kN case, (c) the 10-kN case, and (d) the 15-kN case.

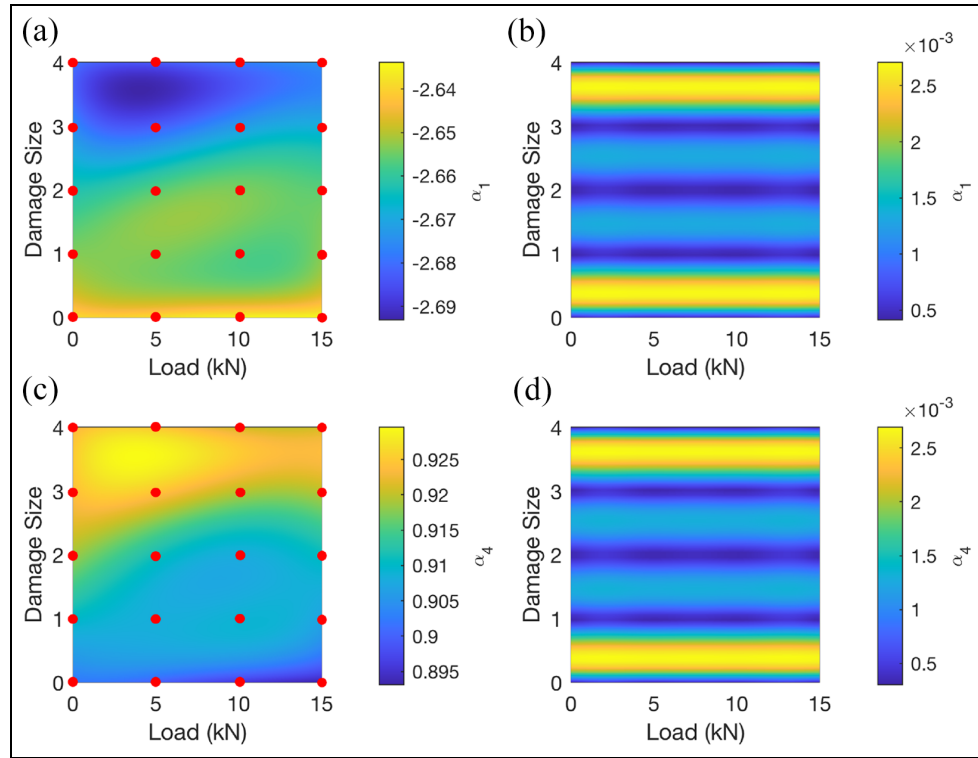


Figure 16. Indicative parameter-based multi-input GPRM predictive moments at $177.7 \mu\text{s}$ for path 2–6: (a) the predictive mean for the first parameter with training data overlaid in red circles, (b) the predictive standard deviation for the first parameter, (c) the predictive mean for the fourth parameter with training data overlaid in red circles, and (d) the predictive standard deviation for the fourth parameter.

GPRM: Gaussian Process regression model.

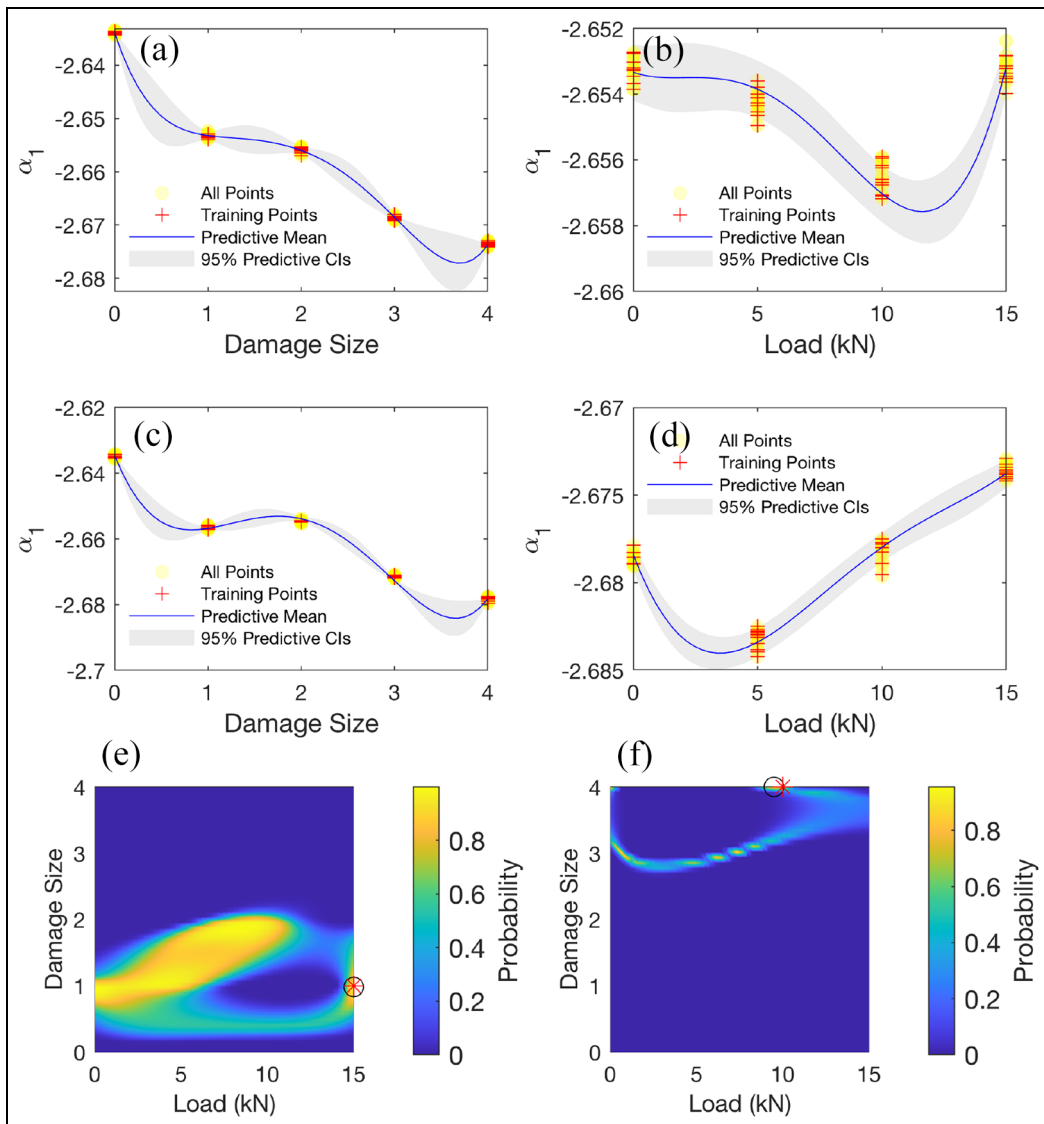


Figure 17. Indicative first parameter-based GPRM predictive moments and prediction probabilities at 177.7 μs for path 2–6 for specific damage and load states: (a) evolution of the first parameter with damage size at 15 kN; (b) evolution of the first parameter with load state with one attached weight; (c) evolution of the first parameter with damage size at 10 kN; (d) evolution of the first parameter with load state with four attached weights; (e) prediction probability for the combined states shown in (a) and (b); (f) prediction probability for the combined states shown in c and d. In the last two panels, the red asterisk indicates the true state while the black circle indicates the state with the highest prediction probability.
GPRM: Gaussian Process regression model.

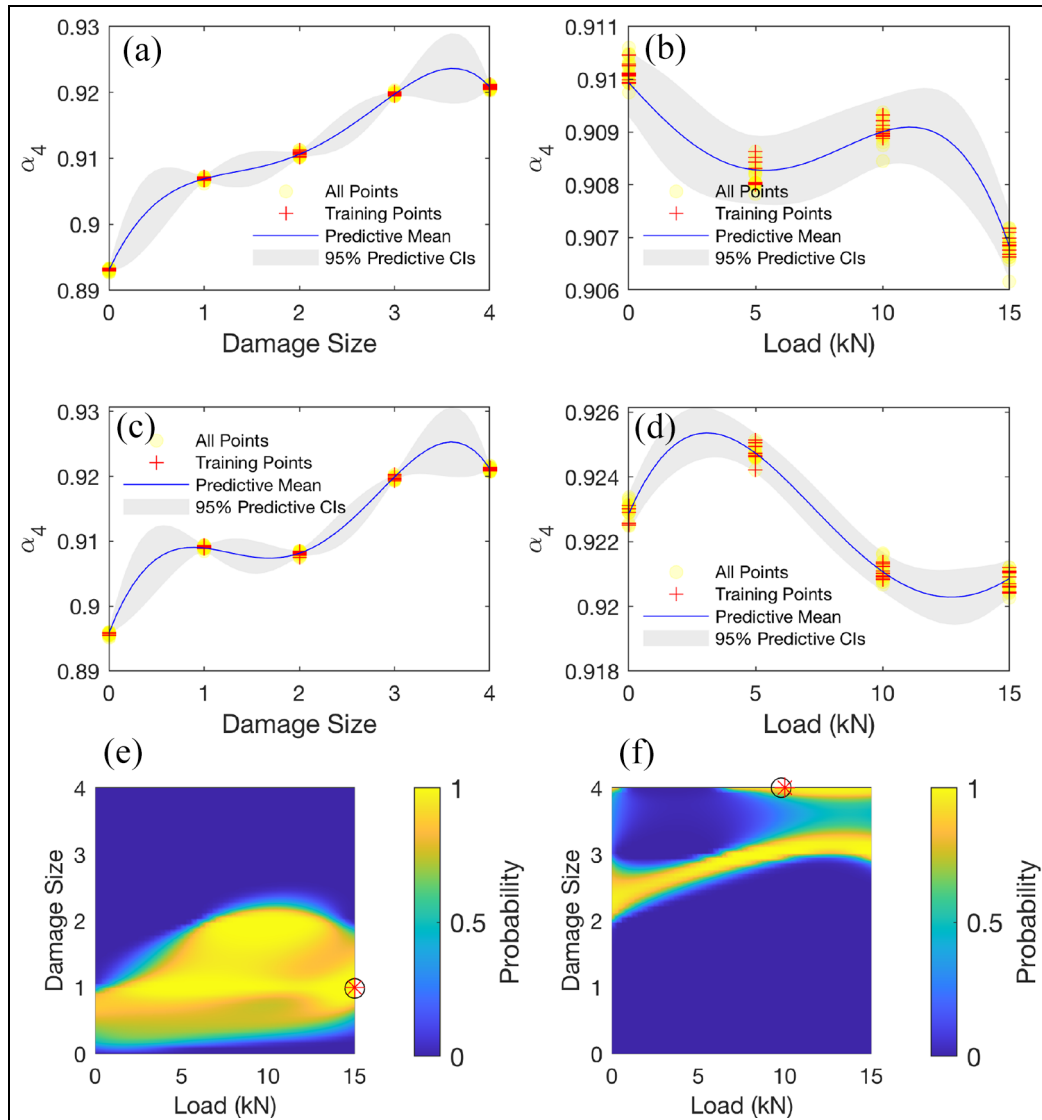


Figure 18. Indicative fourth parameter-based GPRM predictive moments and prediction probabilities at $177.7 \mu\text{s}$ for path 2–6 for specific damage and load states: (a) evolution of the fourth parameter with damage size at 15 kN, (b) evolution of the fourth parameter with load state with one attached weight, (c) evolution of the fourth parameter with damage size at 10 kN, (d) evolution of the fourth parameter with load state with four attached weights, (e) prediction probability for the combined states shown in a and b, and (f) prediction probability for the combined states shown in c and d. In the last two panels, the red asterisk indicates the true state while the black circle indicates the state with the highest prediction probability.
GPRM: Gaussian Process regression model.

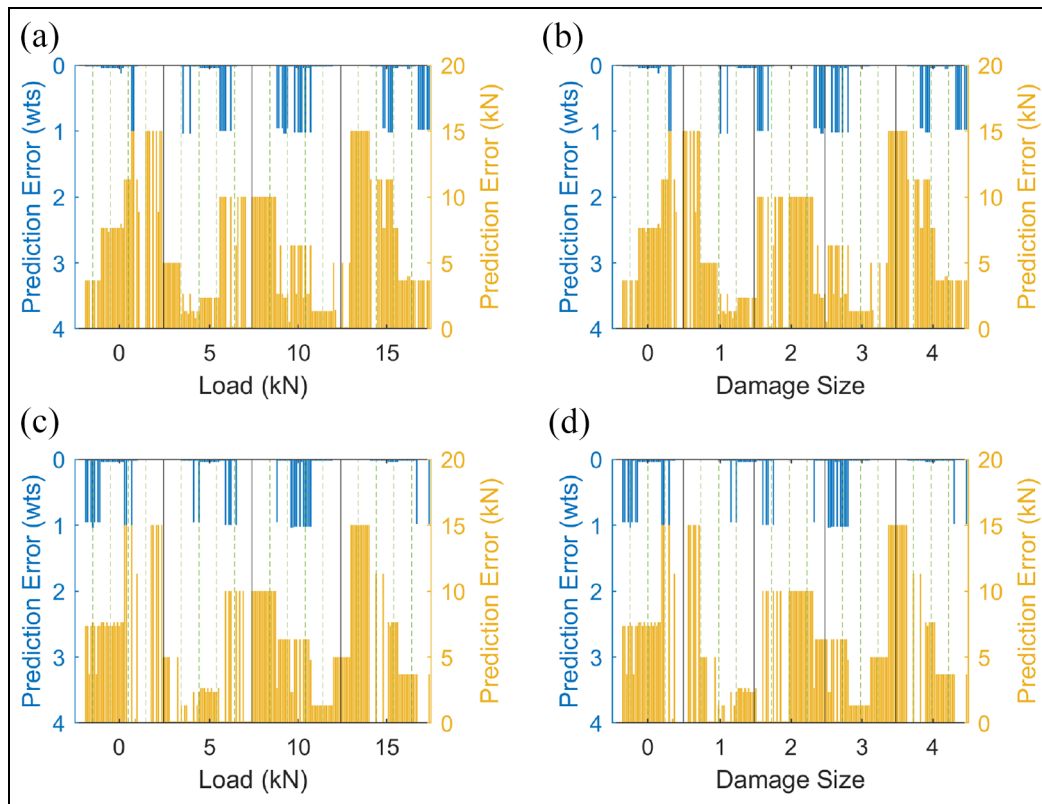


Figure 19. Parameter-based multi-input GPRM prediction errors in damage size and loading state predictions at $177.7 \mu\text{s}$ for path 2–6: (a) prediction errors from the first parameter plotted with respect to load on the x-axis, (b) prediction errors from the first parameter plotted with respect to damage size on the x-axis, (c) prediction errors from the first parameter plotted with respect to load on the x-axis, and (d) prediction errors from the first parameter plotted with respect to damage size on the x-axis. The black solid vertical lines separate regions where each of the values on the x-axis is true, while the green dashed vertical lines separate regions of different damage sizes in a and c and regions of different loading states in b and d.

GPRM: Gaussian Process regression model.

it was shown that both model classes can accurately follow the evolution of parameters with damage size and/or load. While the model showed good damage state predictions and allows for a strong representation of the dynamics of the waves under varying conditions, load-state prediction accuracy was shown to be subpar compared to predictions from damage index-trained GPRMs from the literature. This was attributed to the fact that the time-instant selection algorithm used herein slightly favors damage-size prediction over load-state prediction. To this end, future work with TAR-GPRMs can include adding another layer in the time-instant selection process which also goes through the parameter deviations with respect to loading states first then damage size, and then selecting the time instant that is shared amongst all selection strategies. In addition, adding the time vector directly as an input in the GPRM (creating two- or three-dimensional GPRMs) seems to also be a valid approach to fully accessing the potential of TAR-GPRMs, given a batch

GP training strategy can be applied here to allow for the digestion of a large amount of parameter data in this case. Finally, future studies applying the proposed framework should consider more realistic test cases such as cracks/impact damage in metallic/composite coupons and sub-components, as well as damage under varying environmental conditions, for validating the effectiveness of the work presented in this study.

Declaration of conflicting interests

The author(s) declared no potential conflicts of interest with respect to the research, authorship, and/or publication of this article.

Funding

The author(s) disclosed receipt of the following financial support for the research, authorship, and/or publication of this article: This work is carried out at the Rensselaer Polytechnic

Institute under the Vertical Lift Research Center of Excellence Program, grant number W911W61120012, with Dr Mahendra Bhagwat and Dr William Lewis as Technical Monitors. This work has also been supported by the US Air Force Office of Scientific Research grant “Formal Verification of Stochastic State Awareness for Dynamic Data-Driven Intelligent Aerospace Systems” (FA9550-19-1-0054) with Program Officer Dr Erik Blasch.

ORCID iDs

Ahmad Amer  <https://orcid.org/0009-0000-1866-0080>
 Fotis Kopsaftopoulos  <https://orcid.org/0000-0001-8795-3725>

References

- Dong T and Kim NH. Cost-effectiveness of structural health monitoring in fuselage maintenance of the civil aviation industry. *Aerospace* 2018; 5: 87.
- Biondini F and Frangopol DM. Life-cycle performance of deteriorating structural systems under uncertainty: review. *J Struct Eng* 2016; 142(9): F4016001.
- Frangopol DM and Soliman M. Life-cycle of structural systems: recent achievements and future directions. *Struct Infrastruct Eng* 2016; 12(1): 1–20.
- Frangopol DM and Maute K. Life-cycle reliability-based optimization of civil and aerospace structures. *Struct Infrastruct Eng* 2003; 81(1): 397–410.
- Gomes GF, Mendéz YAD, Alexandrino PSL, et al. The use of intelligent computational tools for damage detection and identification with an emphasis on composites – a review. *Compos Struct* 2018; 196: 44–54.
- Jordan S, Moore J, Hovet S, et al. State-of-the-art technologies for UAV inspections. *IET Radar, Sonar Navig* 2018; 12(2): 151–164.
- Cawley P. Structural health monitoring: closing the gap between research and industrial deployment. *Struct Health Monit* 2018; 17(5): 1225–1244.
- Khodaei ZS and Aliabadi MHF. *Damage detection and characterization with piezoelectric transducers: active sensing*, chapter 1. Singapore: World Scientific, pp. 1–46.
- Yadav SK, Chung H, Kopsaftopoulos FP, et al. Damage quantification of active sensing acousto-ultrasound-based SHM based on a multi-path unit-cell approach. In: *Proceedings of the 11th international workshop on structural health monitoring (IWSHM 2017)*, Palo Alto, CA, USA, September 2017. Lancaster, Pennsylvania: DEStech Publications, Inc.
- Mitra M and Gopalakrishnan S. Guided wave based structural health monitoring: a review. *Smart Mater Struct* 2016; 25: 053001.
- Diamanti K and Soutis C. Structural health monitoring techniques for aircraft composite structures. *Prog Aerosp Sci* 2010; 46(8): 342–352.
- Farrar CR and Worden K. An introduction to structural health monitoring. *Philos Trans Math Phys Eng Sci* 2007; 365: 303–315.
- Amer A and Kopsaftopoulos FP. Probabilistic active sensing acousto-ultrasound SHM based on non-parametric stochastic representations. In: *Proceedings of the vertical flight society 75th annual forum & technology display*, Philadelphia, PA, USA, May 2019. Fairfax, Virginia: The Vertical Flight Society.
- Amer A and Kopsaftopoulos FP. Probabilistic damage quantification via the integration of non-parametric time-series and Gaussian process regression models. In: *Proceedings of the 12th international workshop on structural health monitoring (IWSHM 2019)*, Palo Alto, CA, USA, September 2019, pp. 2384–2393. Lancaster, Pennsylvania: DEStech Publications, Inc.
- Ahmed S and Kopsaftopoulos FP. Uncertainty quantification of guided waves propagation for active sensing structural health monitoring. In: *Proceedings of the vertical flight society 75th annual forum & technology display*, Philadelphia, PA, USA, May 2019. Fairfax, Virginia: The Vertical Flight Society.
- Lu Y and Michaels JE. A methodology for structural health monitoring with diffuse ultrasonic waves in the presence of temperature variations. *Ultrasonics* 2005; 43(9): 717–731.
- Konstantinidis G, Drinkwater BW and Wilcox PD. The temperature stability of guided wave structural health monitoring systems. *Smart Mater Struct* 2006; 27: 967–976.
- Putkis O and Croxford AJ. Continuous baseline growth and monitoring for guided wave SHM. *Smart Mater Struct* 2013; 22: 055029.
- Clarke T, Cawley P, Wilcox PD, et al. Evaluation of the damage detection capability of a sparse-array guided-wave SHM system applied to a complex structure under varying thermal conditions. *IEEE Trans Ultrason Ferroelectr Freq Control* 2009; 56: 2666–2678.
- Xu C-b, Yang Zb, Chen Xf, et al. A guided wave dispersion compensation method based on compressed sensing. *Mech Syst Signal Process* 2018; 103: 89–104.
- Roy S, Lonkar K, Janapati V, et al. A novel physics-based temperature compensation model for structural health monitoring using ultrasonic guided waves. *Struct Health Monit* 2014; 13(3): 321–342.
- Wang Y, Wang G, Wu D, et al. An improved matching pursuit-based temperature and load compensation method for ultrasonic guided wave signals. *IEEE Access* 2020; 8: 67530–67541.
- Roy S, Ladpli P and Chang F-K. Load monitoring and compensation strategies for guided waves based structural health monitoring using piezoelectric transducers. *J Sound Vibr* 2015; 351: 206–220.
- Douglass ACS and Harley JB. Dynamic time warping temperature compensation for guided wave structural health monitoring. *IEEE Trans Ultrason Ferroelectr Freq Control* 2018; 65(5): 851–861.
- Amer A, Roy S and Kopsaftopoulos FP. Probabilistic SHM under varying loads via the integration of Gaussian Process Regression and physics-based guided-wave propagation models. In: *Proceedings of the AIAA SciTech*

- 2021 forum, Virtual Event, January 2021. Reston, Virginia: American Institute of Aeronautics and Astronautics.
- 26. Janapati V, Kopsaftopoulos F, Li F, et al. Damage detection sensitivity characterization of acousto-ultrasound-based structural health monitoring techniques. *Struct Health Monitor* 2016; 15(2): 143–161.
 - 27. Ravi SK, Dong P and Wei Z. Data-driven modeling of multiaxial fatigue in frequency domain. *Mar Struct* 2022; 84: 103201.
 - 28. Liu C, Harley JB, Bergés M, et al. Robust ultrasonic damage detection under complex environmental conditions using singular value decomposition. *Ultrasonics* 2015; 58: 75–86.
 - 29. Tibaduiza DA, Mujica LE, Rodellar J, et al. Structural damage detection using principal component analysis and damage indices. *J Intell Mater Syst Struct* 2016; 27(2): 233–248.
 - 30. Yang K, Kim S, Yue R, et al. Long-term guided wave structural health monitoring in an uncontrolled environment through long short-term principal component analysis. *Struct Health Monit* 2021; 21: 1–17.
 - 31. Su Z and Ye L. Lamb wave-based quantitative identification of delamination in CF/EP composite structures using artificial neural algorithm. *Compos Struct* 2004; 66: 627–637.
 - 32. Fenza AD, Sorrentino A and Vitiello P. Application of artificial neural networks and probability ellipse methods for damage detection using Lamb waves. *Compos Struct* 2015; 133: 390–403.
 - 33. Dib G, Karpenko O, Koricho E, et al. Ensembles of novelty detection classifiers for structural health monitoring using guided waves. *Smart Mater Struct* 2018; 27: 015003.
 - 34. Agarwal S and Mitra M. Lamb wave based automatic damage detection using matching pursuit and machine learning. *Smart Mater Struct* 2014; 23: 085012.
 - 35. Eybpoosh M, Berges M and Noh HY. Sparse representation of ultrasonic guided-waves for robust damage detection in pipelines under varying environmental and operational conditions. *Struct Control Health Monit* 2016; 23: 369–391.
 - 36. Wang F, Huo L and Song G. A piezoelectric active sensing method for quantitative monitoring of bolt loosening using energy dissipation caused by tangential damping based on the fractal contact theory. *Smart Mater Struct* 2018; 27: 015023.
 - 37. Lize E, Rebillat M, Mechbal N, et al. Optimal dual-PZT and network design for baseline-free SHM of complex anisotropic composite structures. *Smart Mater Struct* 2018; 27: 115018.
 - 38. Hua J, Cao X, Yi Y, et al. Time-frequency damage index of broadband lamb wave for corrosion inspection. *J Sound Vibr* 2020; 464: 114985.
 - 39. Qiu L, Yuan S, Mei H, et al. An improved Gaussian mixture model for damage propagation monitoring of an aircraft wing spar under changing structural boundary conditions. *Sensors* 2016; 16(3): 291.
 - 40. Ren Y, Qui L, Yuan S, et al. Gaussian mixture model and delay-and-sum based 4D imaging of damage in aircraft composite structures under time-varying conditions. *Mech Syst Signal Process* 2020; 135: 106390.
 - 41. Zhang J, Yuan S and Chen J. Guided wave-hidden Markov model for on-line crack evaluation of a full-scale aircraft. *Aerospace Sci Technol* 2021; 117: 1067976.
 - 42. He S and Ng C-T. A probabilistic approach for quantitative identification of multiple delaminations in laminated composite beams using guided waves. *Eng Struct* 2016; 127: 602–614.
 - 43. Cantero-Chinchilla S, Malik MK, Chronopoulos D, et al. On-line updating Gaussian process measurement model for crack prognosis using the particle filter. *Compos Struct* 2021; 267: 113849.
 - 44. Ahmed S and Kopsaftopoulos F. Stochastic identification of guided wave propagation under ambient temperature via non-stationary time series models. *Sensors* 2021; 21: 5672.
 - 45. Fassois SD and Kopsaftopoulos FP. Statistical time series methods for vibration based structural health monitoring. In: Ostachowicz W and Guemes A (eds) *New trends in structural health monitoring*, chapter 4. Springer, 2013, pp. 209–264. Vienna: Springer.
 - 46. Fassois SD and Sakellariou JS. Statistical time series methods for structural health monitoring. In: Boller C, Chang FK and Fujino Y (eds) *Encyclopedia of structural health monitoring*. Hoboken, New Jersey: John Wiley & Sons Ltd., 2009, pp. 443–472.
 - 47. Kopsaftopoulos FP and Fassois SD. Scalar and vector time series methods for vibration based damage diagnosis in a scale aircraft skeleton structure. *J Theor Appl Mech* 2011; 49(3): 727–756.
 - 48. Poulimenos AG. *Modeling of non-stationary vibration signals via Functional Series (FS) TARMA models*. PhD thesis, Department of Mechanical Engineering and Aeronautics, University of Patras, Greece, 2007.
 - 49. Avendano-Valencia D and Fassois SD. Robust fault detection based on multiple functional series TAR models for structures with time-dependent dynamics. In: *EWSHM – 7th European workshop on structural health monitoring*, Inria, Université de Nantes, Nantes, France, July 2014. France: HAL open science.
 - 50. Spiridonakos M, Poulimenos A and Fassois S. Output-only identification and dynamic analysis of time-varying mechanical structures under random excitation: a comparative assessment of parametric methods. *J Sound Vibr* 2010; 329(7): 768–785.
 - 51. Kopsaftopoulos FP and Fassois SD. Vector-dependent functionally pooled ARX models for the identification of systems under multiple operating conditions. In: *Proceedings of the 16th IFAC symposium on system identification, (SYSID)*, Brussels, Belgium, July 2012. Amsterdam, Netherlands: Elsevier.
 - 52. Kopsaftopoulos F and Fassois SD. Vibration based health monitoring for a lightweight truss structure: experimental assessment of several statistical time series methods. *Mech Syst Signal Process* 2010; 24: 1977–1997.

53. Kopsaftopoulos F, Nardari R, Li Y-H, et al. A stochastic global identification framework for aerospace structures operating under varying flight states. *Mech Syst Signal Process* 2018; 98: 425–447.
54. Avendaño-Valencia LD and Fassois SD. Natural vibration response based damage detection for an operating wind turbine via Random Coefficient Linear Parameter Varying AR modeling. *J Phys Conf Ser* 2015; 628: 012073.
55. Avendaño-Valencia L, Barahona B, Hoelzl C, et al. Operational regime clustering for the construction of PCE-based surrogates of operational wind turbines. In: *Proceedings of the 7th international conference on advances in experimental structural engineering*, 2017, pp. 961–964. Pavia, Italy; Eucentre Foundation.
56. Avendaño-Valencia LD, Chatzi EN, Koo KY, et al. Gaussian process time-series models for structures under operational variability. *Front Built Environ* 2017; 3: pp. 69.
57. Abdessalem AB, Dervilis N, Wagg DJ, et al. Automatic kernel selection for Gaussian processes regression with approximate Bayesian computation and sequential Monte Carlo. *Front Built Environ* 2017; 3: 52.
58. Bull L, Rogers T, Dervilis N, et al. A Gaussian process form for population-based structural health monitoring. In: *Proceedings of the 13th international conference on damage assessment of structures (DAMAS 2019)*, Springer, Porto, Portugal, September 2019. Singapore: Springer Nature.
59. Gonzaga P, Dervilis N, Worden K, et al. Structural health monitoring: a review of uncertainty quantification methods in wind turbine systems. In: *Proceedings of the 12th international workshop on structural health monitoring (IWSHM 2019)*, Palo Alto, CA, USA, September 2019. Lancaster, Pennsylvania: DEStech Publications, Inc.
60. Lázaro-Gredilla M, Titsias MK, Verrelst J, et al. Estimation of vegetation chlorophyll content with variational heteroscedastic Gaussian processes. In: *2013 IEEE international geoscience and remote sensing symposium-IGARSS*, 2013, pp. 3010–3013. Piscataway, New Jersey: IEEE.
61. Qizhi T, Jingzhou X, Jianting Z, et al. Structural damage identification method based on AR-GP model. *J Vib Shock* 2021; 40(9): 4341.
62. Avendaño-Valencia L, Tatsis K and Chatzi E. Gaussian process vector AR surrogates for identification of structures under varying operational conditions. In: *8th Conference on computational stochastic mechanics (CSM8)*, Paros, Greece, June 2018. Singapore: Research Publishing (S) Pte. Ltd.
63. Worden K, Manson G and Cross EJ. On Gaussian process NARX models and their higher-order frequency response functions. In: Koziel S, Leifsson L and Yang X-S (eds) *Solving computationally expensive engineering problems*. Cham, Switzerland: Springer, 2014, pp. 315–335.
64. Fuentes R, Cross EJ, Halfpenny A, et al. Autoregressive Gaussian process for structural damage detection. *ISMA* 2014; 2014: 469–484.
65. Worden K, Rogers T and Cross E. Identification of non-linear wave forces using Gaussian process NARX models. In: Kerschen G (ed.) *Nonlinear dynamics, volume 1. Conference proceedings of the society for experimental mechanics series*. Springer, 2017. pp. 203–221. Cham, Switzerland: Springer.
66. Amer A and Kopsaftopoulos FP. Towards unified probabilistic rotorcraft damage detection and quantification via non-parametric time series and Gaussian process regression models. In: *Proceedings of the vertical flight society 76th annual forum & technology display*, Virginia Beach, VA, USA, October 2020. Fairfax, Virginia: The Vertical Flight Society.
67. Amer A, Ahmed A and Kopsaftopoulos FP. Active-sensing structural health monitoring via statistical learning: an experimental study under varying damage and loading states. In: *Special volume, 10th European workshop on structural health monitoring (EWSHM 2022)*. Springer, 2020. Switzerland: Springer Nature.
68. Poulimenos A and Fassois S. Parametric time-domain methods for non-stationary random vibration modelling and analysis—a critical survey and comparison. *Mech Syst Signal Pr* 2005; 20(4): 763–816.
69. Sotiriou D, Kopsaftopoulos F and Fassois S. An adaptive time-series probabilistic frame work for 4-D trajectory conformance monitoring. *IEEE Trans Intell Transp Syst* 2016; 17(6): 1606–1616.
70. Ljung L. System identification. System identification: theory for the user. 2nd ed. Upper Saddle River, NJ: Prentice-Hall, 1999.
71. Shi G (ed.). Kriging. In: *Data mining and knowledge discovery for geoscientists*, chapter 8. Oxford, UK: Elsevier, 2014, pp. 238–274.
72. Kennedy MC and O'Hagan A. Bayesian calibration of computer models. *J Roy Statistical Soc Series B* 2002; 63(3): 425–464.
73. Jo S, Le J, Page G, et al. Spatial Species Sampling and Product Partition Models. In: Mitra R and Müller P (eds) *Nonparametric Bayesian Inference in Biostatistics*. Frontiers in Probability and the Statistical Sciences. Cham: Springer, 2015.
74. Baukol CR, McDonald RA and Delmas N. A user friendly interface for Gaussian process metamodeling. In: *47th AIAA aerospace science meeting including the new horizons forum and aerospace exposition*. Orlando, FL, 2009, pp. 1–13. Reston, Virginia: American Institute of Aeronautics and Astronautics.
75. Rasmussen CE and Williams CKI (eds). *Gaussian processes for machine learning*. Cambridge, MA: MIT Press, 2006.
76. Rogers T, Gardner P, Dervilis N, et al. Probabilistic modelling of wind turbine power curves with application of heteroscedastic Gaussian process regression. *Renew Energy* 2020; 148: 1124–1136.

77. Moll J, Kathol J, Fritzen CP, et al. Open Guided Waves: online platform for ultrasonic guided wave measurements. *Struct Health Monit* 2019; 18: 1–12.
78. Kopsaftopoulos FP and Fassois SD. Vibration-based structural damage detection and precise assessment via stochastic functionally pooled models. *Key Eng Mater* 2007; 347: 127–132.
79. Yue N and Alibabadi M. Hierarchical approach for uncertainty quantification and reliability assessment of guided wave-based structural health monitoring. *Struct Health Monit* 2021; 20(5): 2274–2299.
80. Schwarz G. Estimating the dimension of a model. *Ann Stat* 1978; 461–464.
81. Akaike H. On newer statistical approaches to parameter estimation and structure determination. *IFAC Proc* 1978; 11(1): 1877–1884.
82. Ahmed S, Amer A, Varela CA, et al. Data-driven state awareness for fly-by-feel aerial vehicles via adaptive time series and Gaussian process regression models. In: *Dynamic data driven applications systems: third international conference, DDDAS 2020*, Boston, MA, USA, October 2–4, 2020. Cham: Springer, 2020, pp. 57–65.
83. Kay SM. *Modern spectral estimation: theory and application*. Hoboken, NJ: Prentice Hall, 1988.

Appendix

Additional results

TAR-GPRM results for path 2–6 in the Al coupon with simulated damage for additional time instants

Single-input GPRMs.

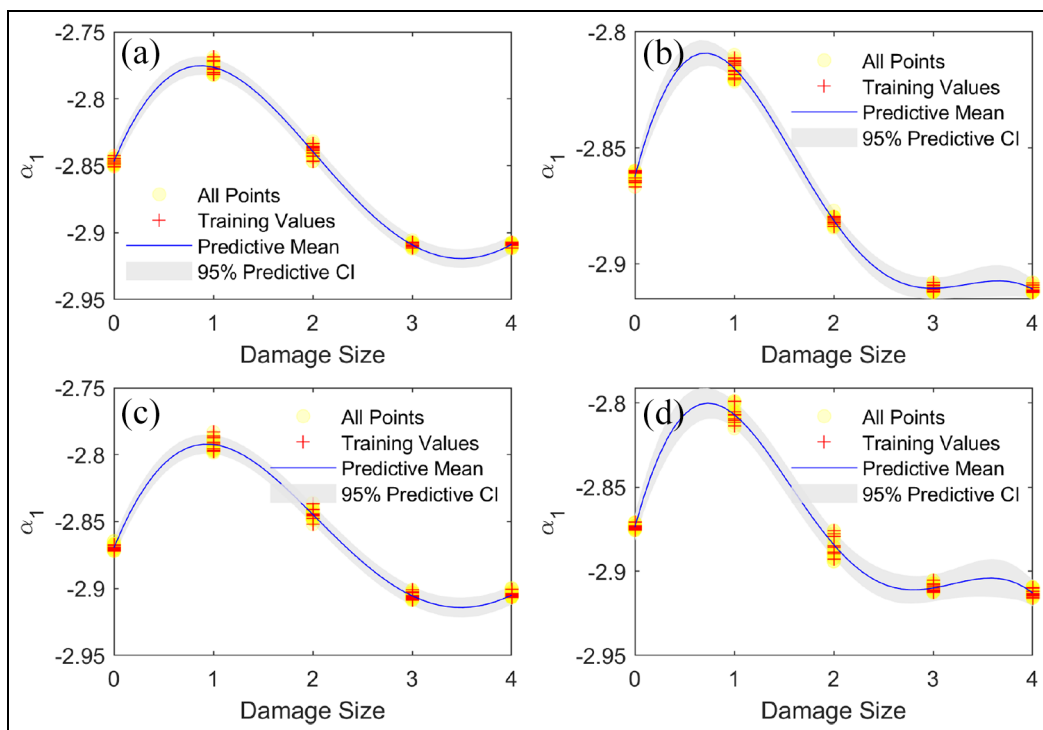


Figure A1. GPRM predictive means and confidence bounds for the first parameter at $129.2 \mu\text{s}$ with damage size under multiple loading states for path 2–6: (a) the no-loading condition, (b) the 5-kN case, (c) the 10-kN case, and (d) the 15-kN case. GPRM: Gaussian Process regression model.

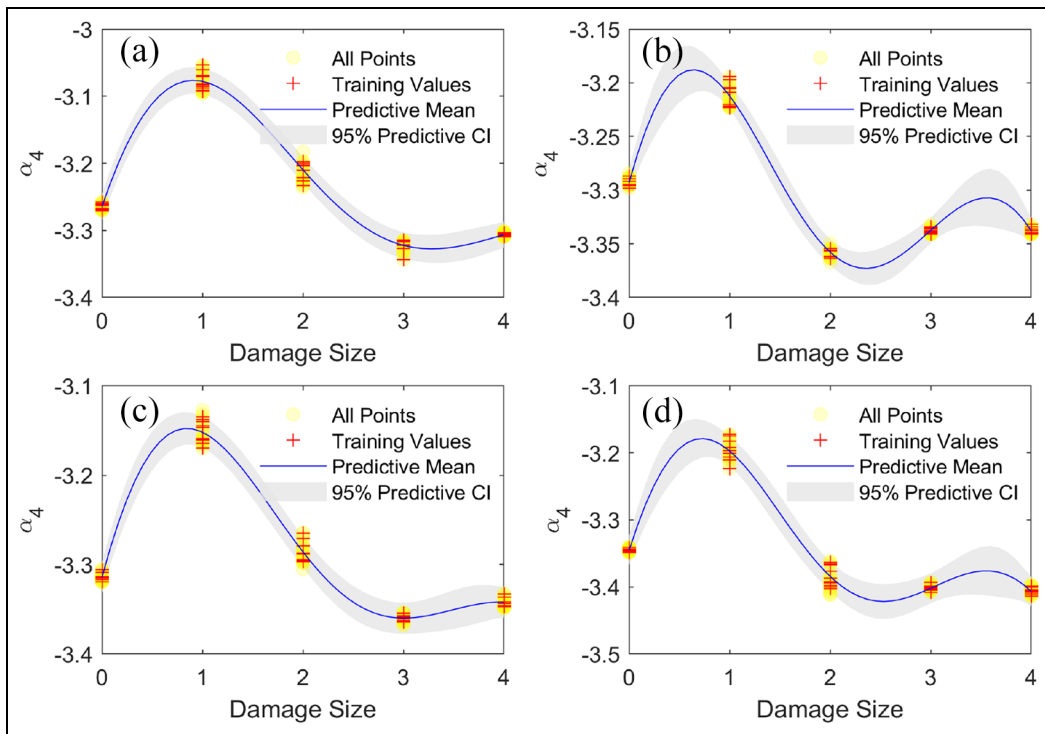


Figure A2. GPRM predictive means and confidence bounds for the fourth parameter at $129.2 \mu s$ with damage size under multiple loading states for path 2–6: (a) the no-loading condition, (b) the 5-kN case, (c) the 10-kN case, and (d) the 15-kN case. GPRM: Gaussian Process regression model.

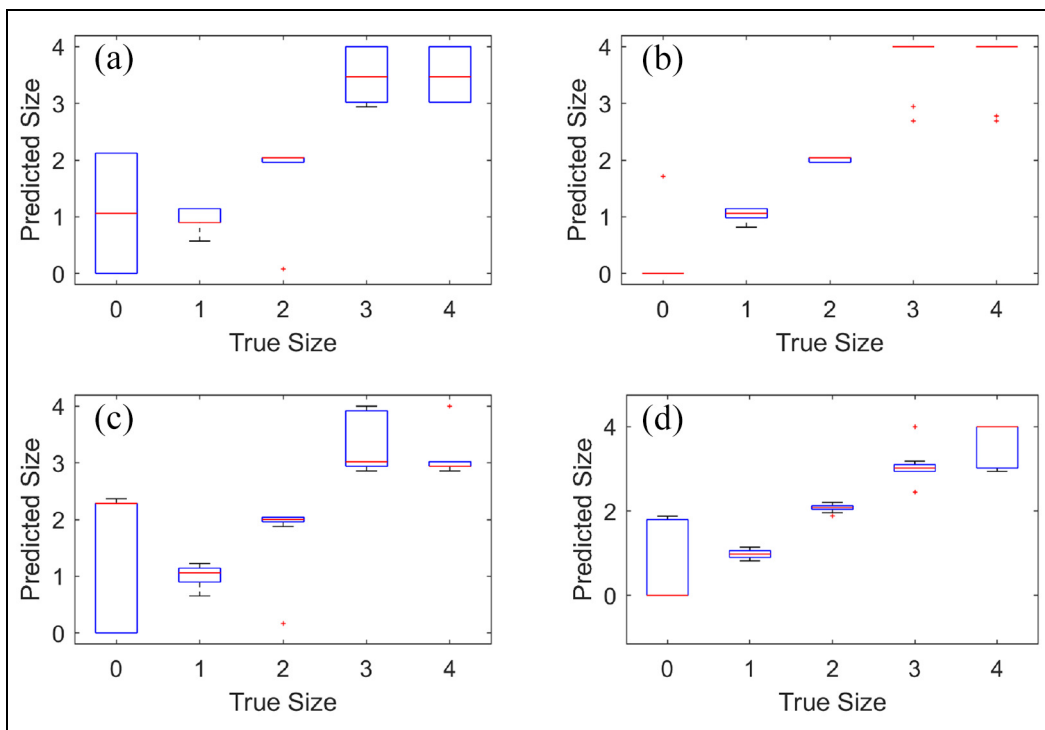


Figure A3. Prediction error boxplots for the fourth parameter at $129.2 \mu s$ with damage size under multiple loading states for path 2–6: (a) the no-loading condition, (b) the 5-kN case, (c) the 10-kN case, and (d) the 15-kN case. GPRM: Gaussian Process regression model.

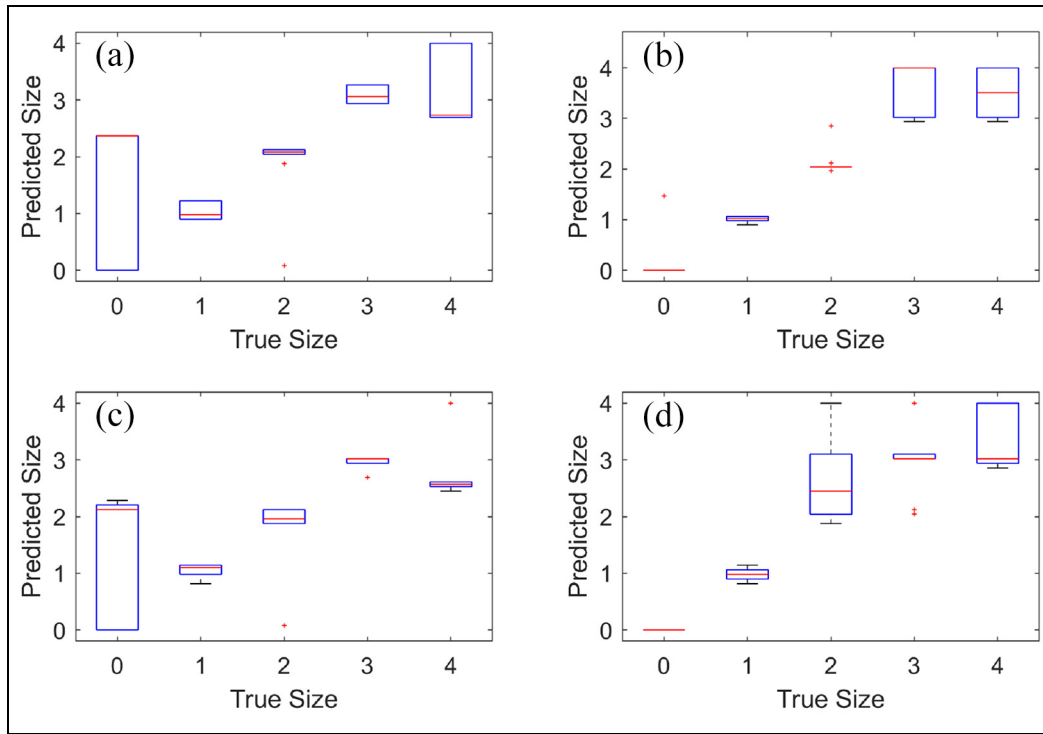


Figure A4. Prediction error boxplots for the fourth parameter at $129.2 \mu\text{s}$ with damage size under multiple loading states for path 2–6: (a) the no-loading condition, (b) the 5-kN case, (c) the 10-kN case, and (d) the 15-kN case.

GPRM: Gaussian Process regression model.

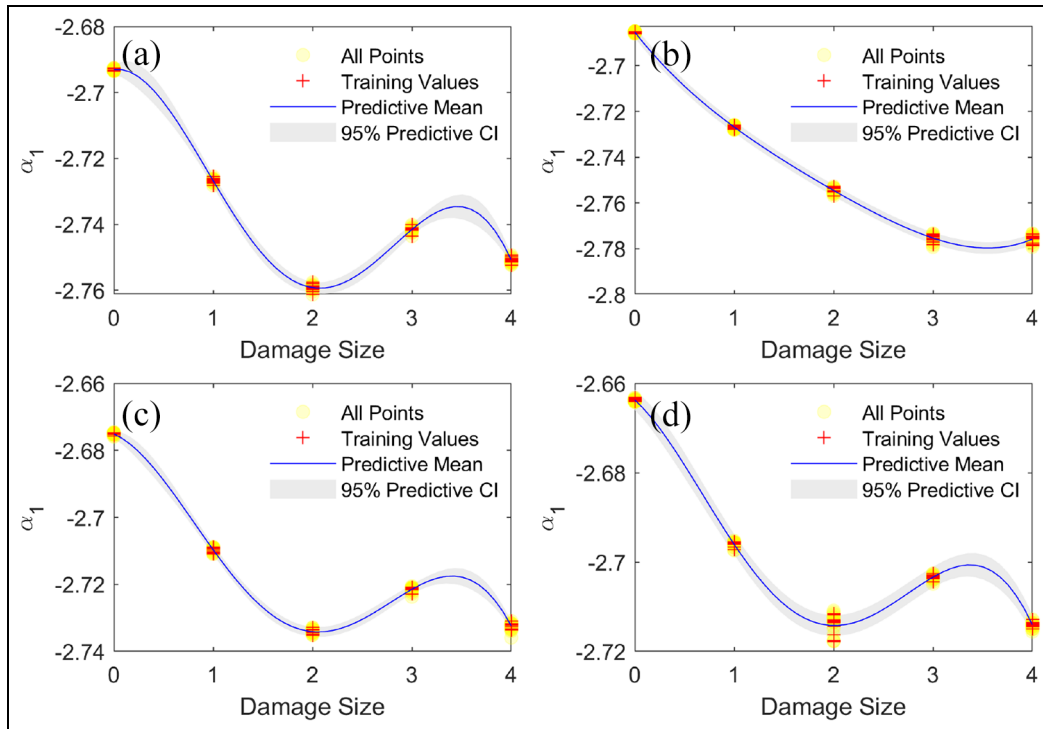


Figure A5. GPRM predictive means and confidence bounds for the first parameter at $188.2 \mu\text{s}$ with damage size under multiple loading states for path 2–6: (a) the no-loading condition, (b) the 5-kN case, (c) the 10-kN case, and (d) the 15-kN case.

GPRM: Gaussian Process regression model.

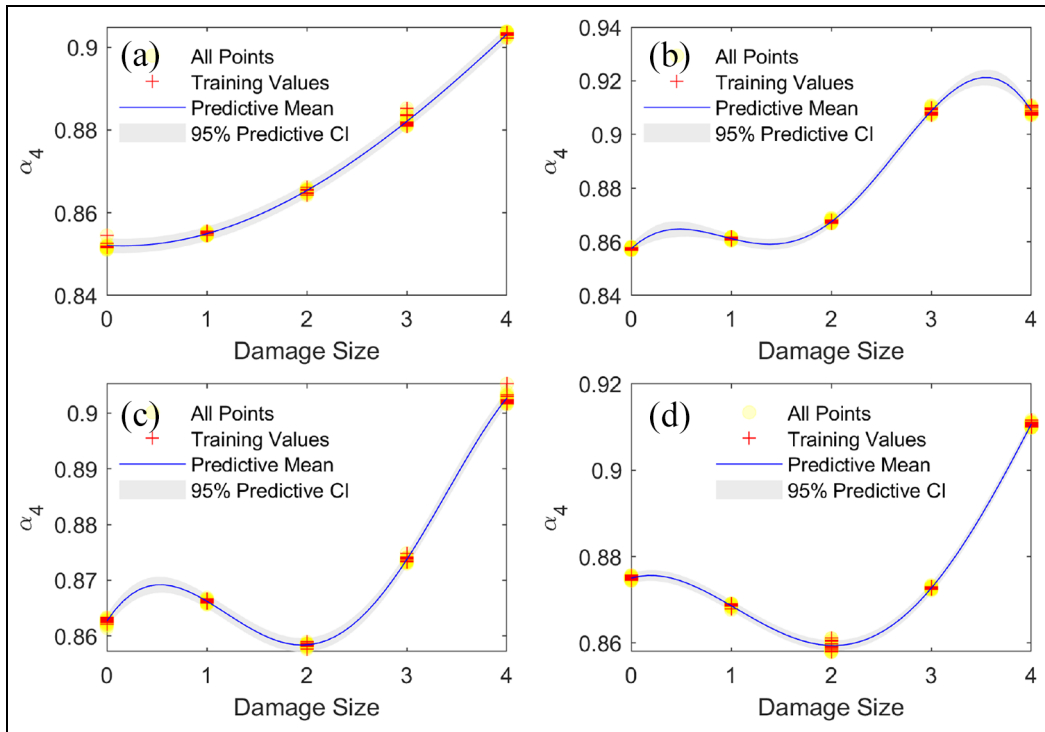


Figure A6. GPRM predictive means and confidence bounds for the fourth parameter at $188.2 \mu\text{s}$ with damage size under multiple loading states for path 2–6: (a) the no-loading condition, (b) the 5-kN case, (c) the 10-kN case, and (d) the 15-kN case. GPRM: Gaussian Process regression model.

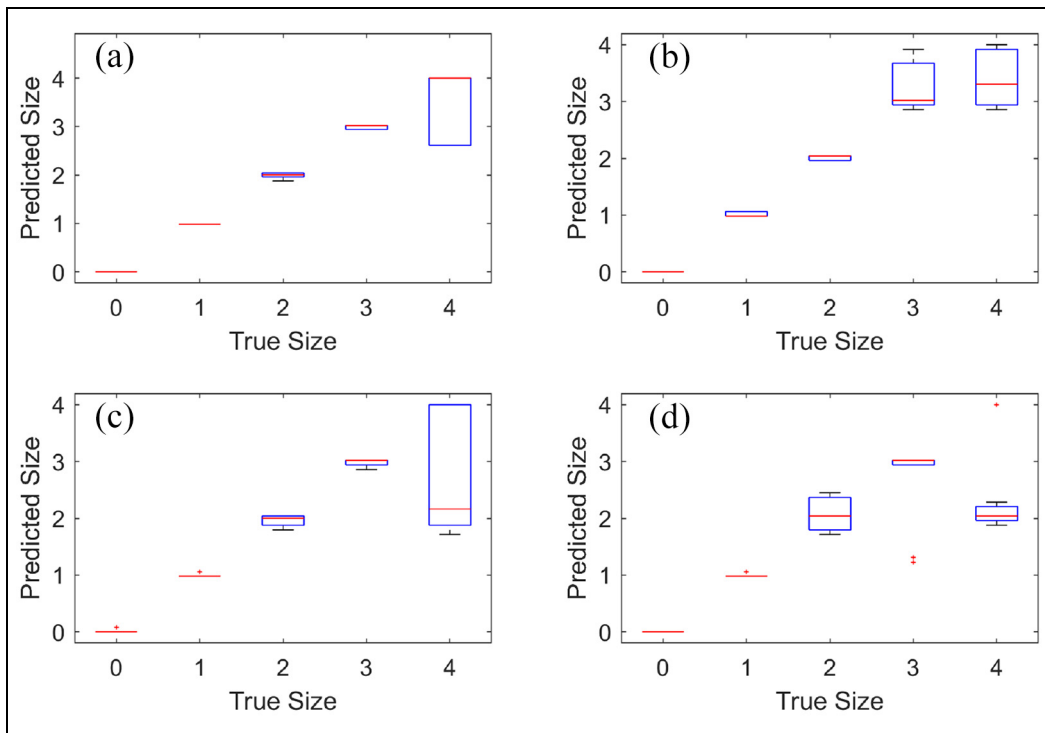


Figure A7. Prediction error boxplots for the first parameter at $188.2 \mu\text{s}$ with damage size under multiple loading states for path 2–6: (a) the no-loading condition, (b) the 5-kN case, (c) the 10-kN case, and (d) the 15-kN case. GPRM: Gaussian Process regression model.

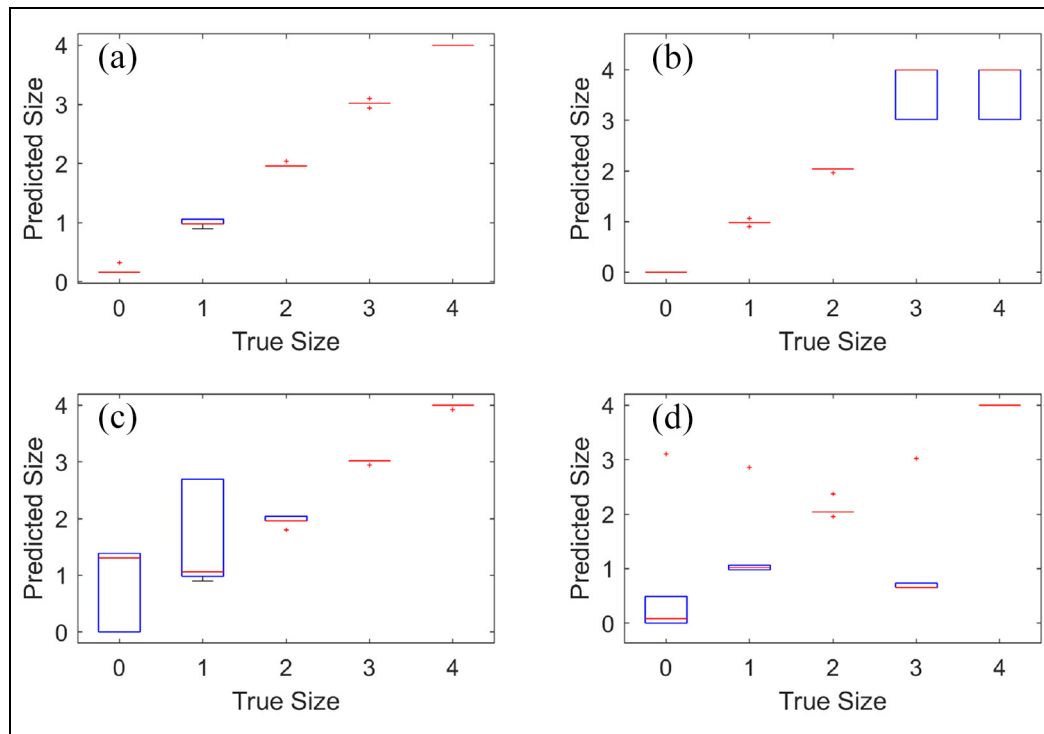


Figure A8. Prediction error boxplots for the fourth parameter at $188.2 \mu\text{s}$ with damage size under multiple loading states for path 2–6: (a) the no-loading condition, (b) the 5-kN case, (c) the 10-kN case, and (d) the 15-kN case.
GPRM: Gaussian Process regression model.

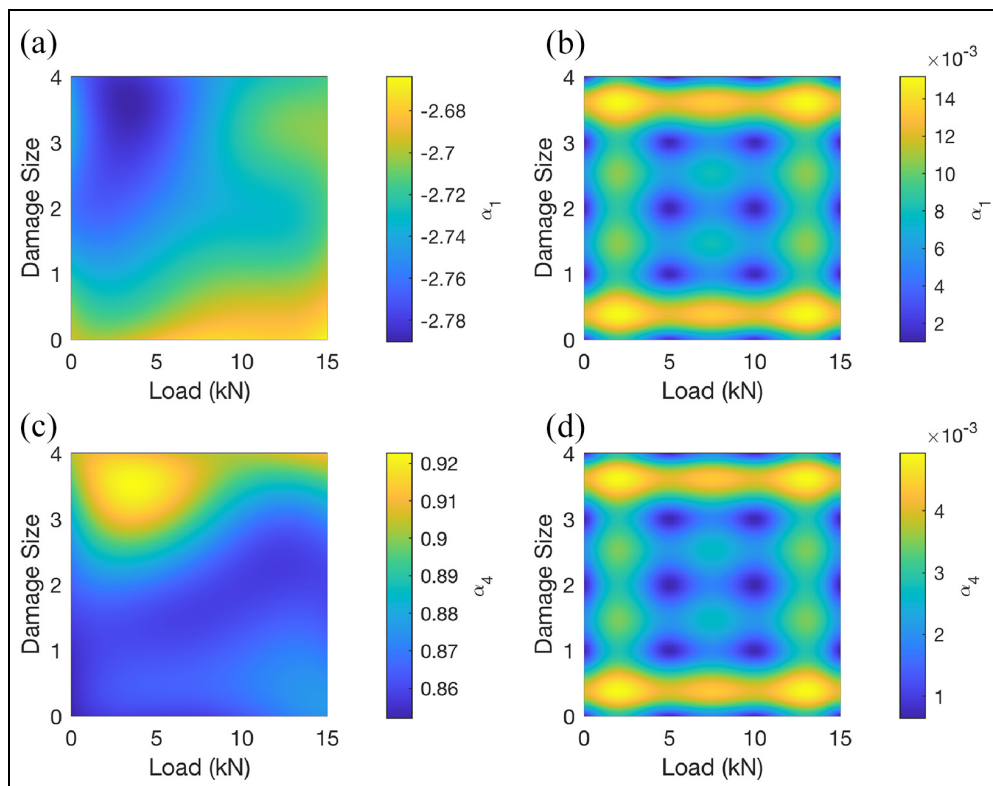


Figure A9. Indicative parameter-based multi-input GPRM predictive moments at $188.2 \mu\text{s}$ for path 2–6: (a) the predictive mean for the first parameter, (b) the predictive standard deviation for the first parameter, (c) the predictive mean for the fourth parameter, and (d) the predictive standard deviation for the fourth parameter.
GPRM: Gaussian Process regression model.

Multi-input GPRMs.

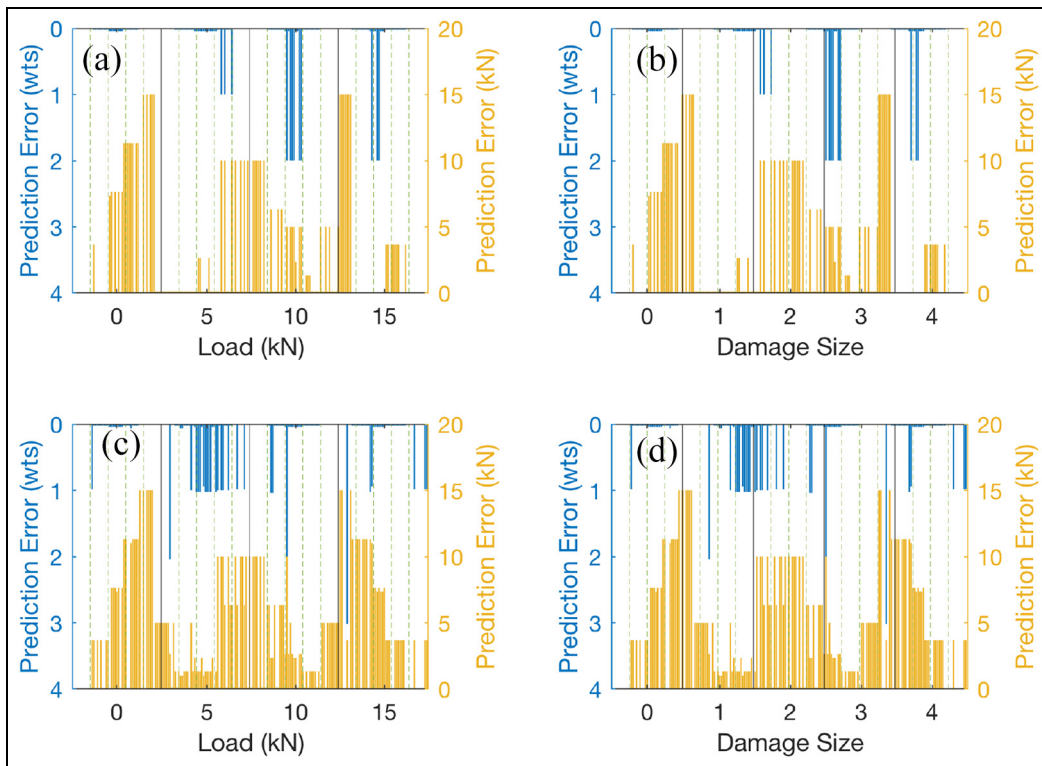


Figure A10. Parameter-based multi-input GPRM prediction errors in damage size and loading state predictions at $188.2 \mu\text{s}$ for path 2–6: (a) prediction errors from the first parameter plotted with respect to load on the x-axis, (b) prediction errors from the first parameter plotted with respect to damage size on the x-axis, (c) prediction errors from the first parameter plotted with respect to load on the x-axis, and (d) prediction errors from the first parameter plotted with respect to damage size on the x-axis. The black solid vertical lines separate regions where each of the values on the x-axis is true, while the green dashed vertical lines separate regions of different damage sizes in a and c and regions of different loading states in b and d.

GPRM: Gaussian Process regression model.

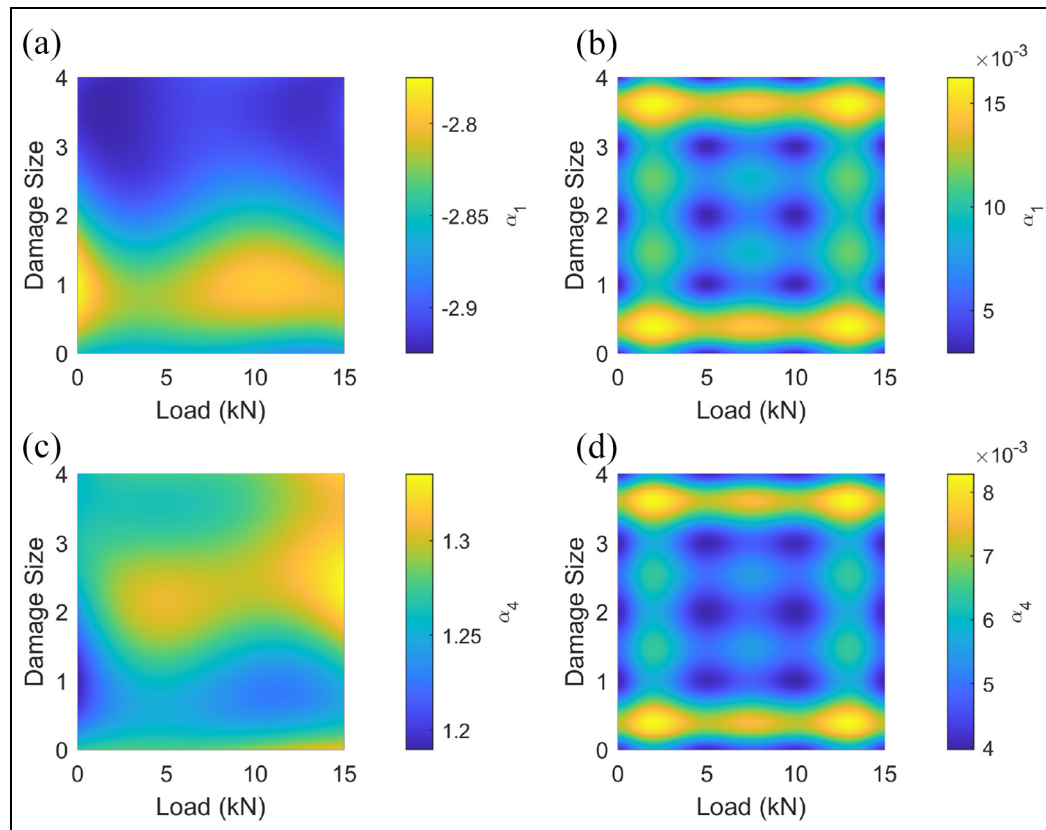


Figure AII. Indicative parameter-based multi-input GPRM predictive moments at $129.2 \mu\text{s}$ for path 2–6: (a) the predictive mean for the first parameter; (b) the predictive standard deviation for the first parameter; (c) the predictive mean for the fourth parameter, and (d) the predictive standard deviation for the fourth parameter.

GPRM: Gaussian Process regression model.

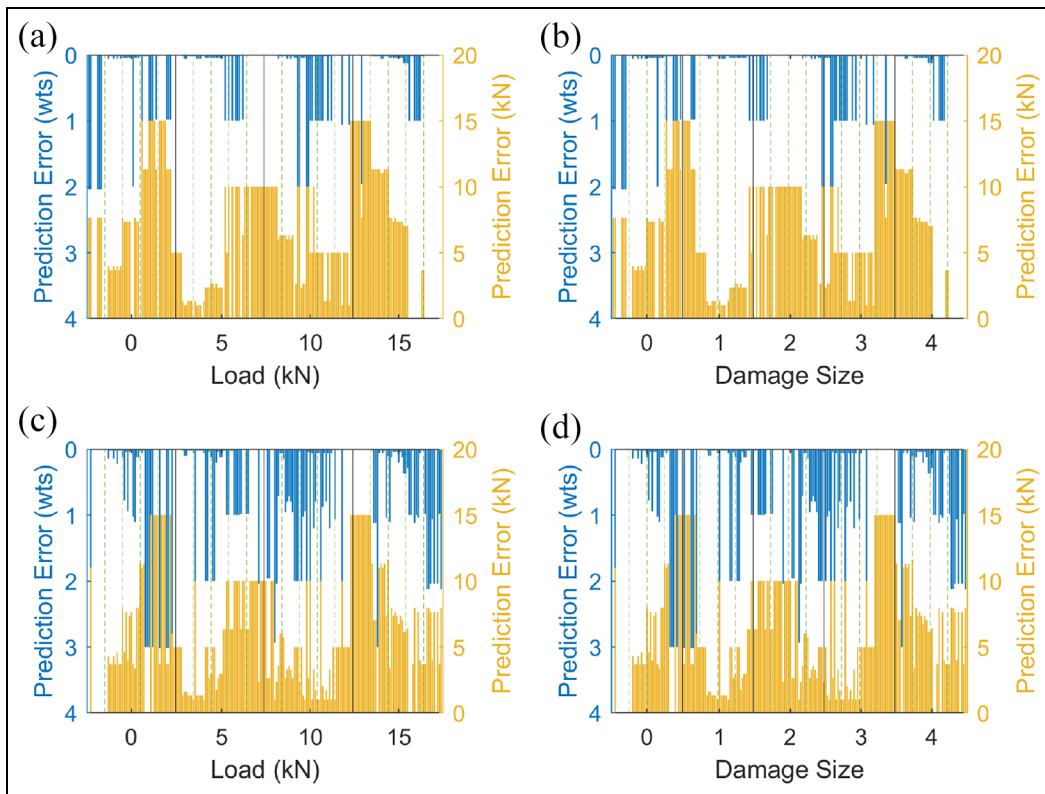


Figure A12. Parameter-based multi-input GPRM prediction errors in damage size and loading state predictions at $129.2 \mu\text{s}$ for path 2–6: (a) prediction errors from the first parameter plotted with respect to load on the x-axis, (b) prediction errors from the first parameter plotted with respect to damage size on the x-axis, (c) prediction errors from the first parameter plotted with respect to load on the x-axis, and (d) prediction errors from the first parameter plotted with respect to damage size on the x-axis. The black solid vertical lines separate regions where each of the values on the x-axis is true, while the green dashed vertical lines separate regions of different damage sizes in a and c and regions of different loading states in b and d. GPRM: Gaussian Process regression model.

TAR-GPRM results for path 2–4 in Al coupon with simulated damage

Table A1. The first 10 time instants*(μs) selected using a single-parameter strategy as described in section ““Selection of time instants” for path 2–4.

61.7	62.2	62.7	63.2	99.2	268.2	268.7	269.2	269.7	310.7
------	------	------	------	------	-------	-------	-------	-------	-------

The blue color highlights the time instants for which the quantification results are presented herein.

*Time instants approximated to the first decimal place

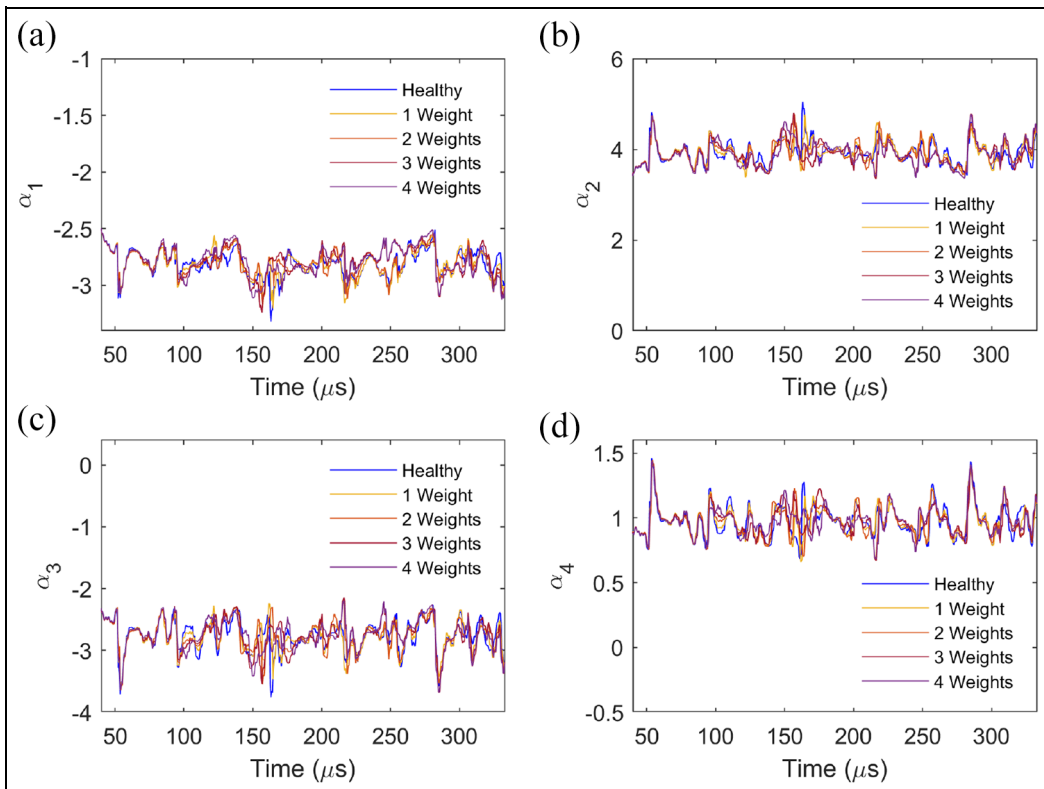


Figure A13. The evolution of the RML-TAR(4)_{0.835} model parameters with damage size (added weights) at a loading state of 0 kN for path 2–4: (a) $\alpha_1(t)$, (b) $\alpha_2(t)$, (c) $\alpha_3(t)$, and (d) $\alpha_4(t)$.

RML: recursive maximum likelihood.

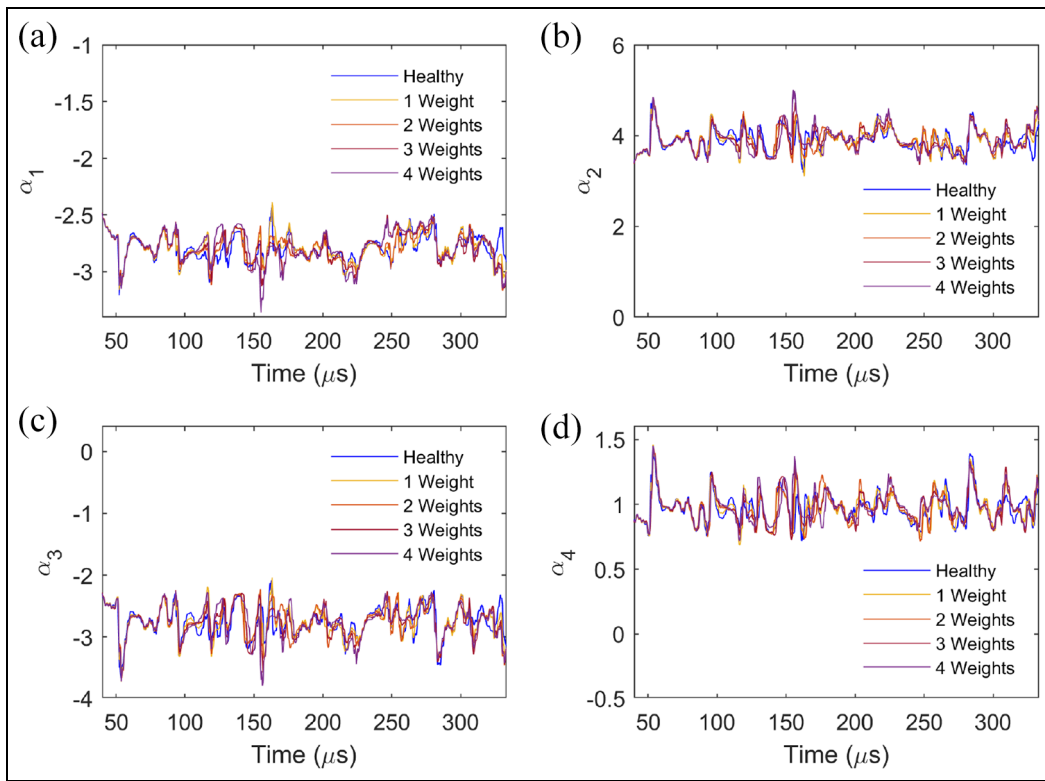


Figure A14. The evolution of the RML-TAR(4)_{0.835} model parameters with damage size (added weights) at a loading state of 10 kN for path 2–4: (a) $\alpha_1(t)$, (b) $\alpha_2(t)$, (c) $\alpha_3(t)$, and (d) $\alpha_4(t)$.
RML: recursive maximum likelihood.

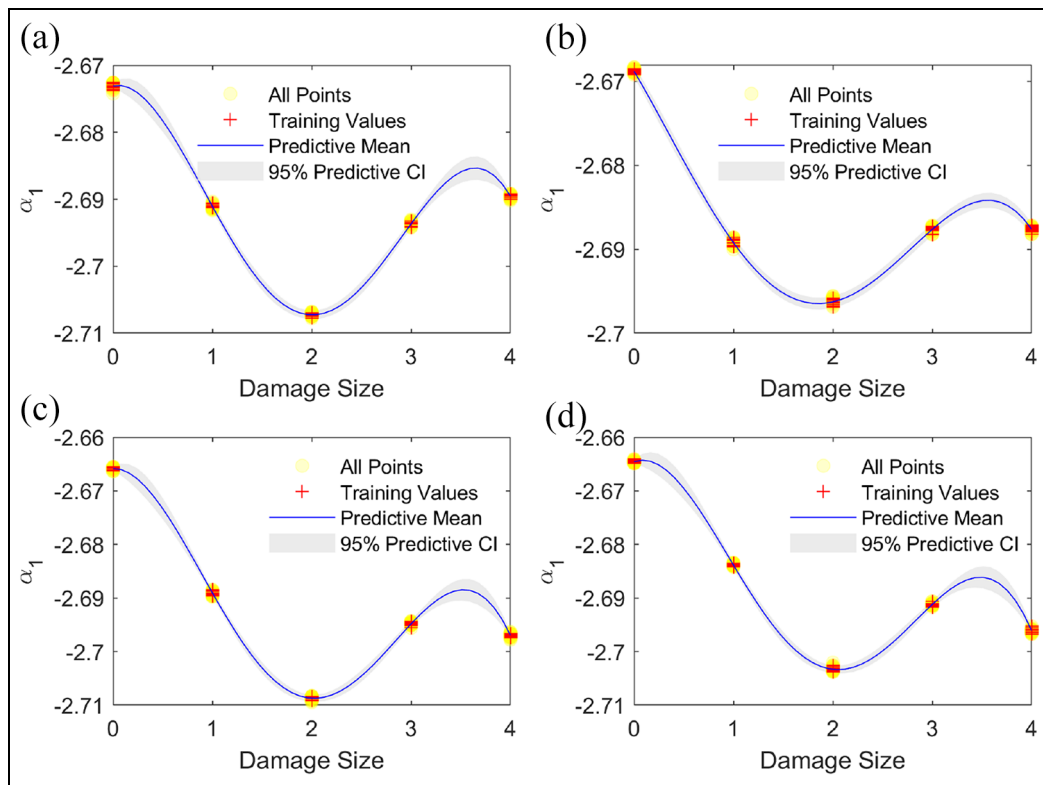
Multi-input GPRMs

Figure A15. GPRM predictive means and confidence bounds for the first parameter at $61.7 \mu\text{s}$ with damage size under multiple loading states for path 2–4: (a) the no-loading condition, (b) the 5-kN case, (c) the 10-kN case, and (d) the 15-kN case.
GPRM: Gaussian Process regression model.

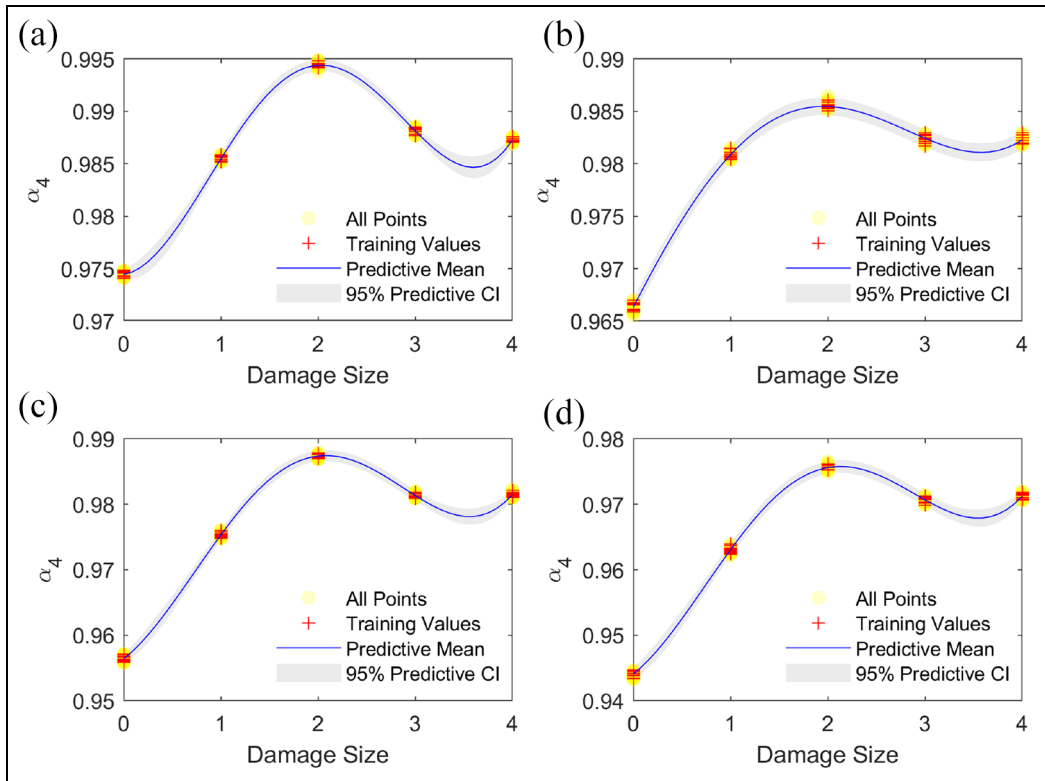


Figure A16. GPRM predictive means and confidence bounds for the fourth parameter at $61.7 \mu\text{s}$ with damage size under multiple loading states for path 2–4: (a) the no-loading condition, (b) the 5-kN case, (c) the 10-kN case, and (d) the 15-kN case.
GPRM: Gaussian Process regression model.

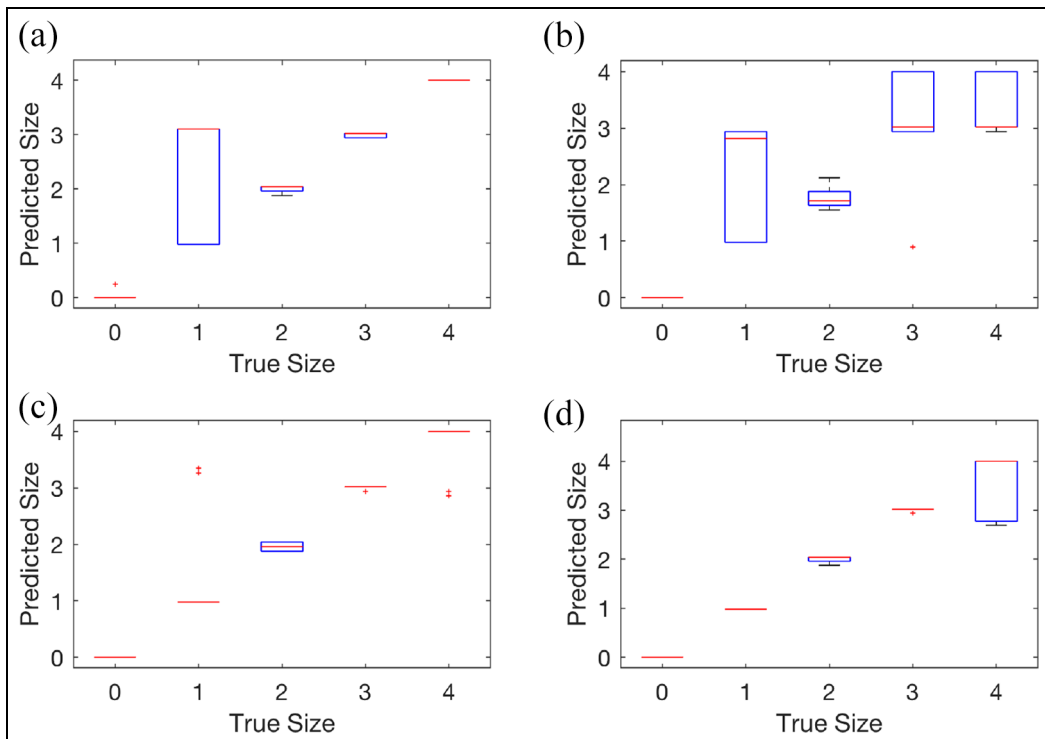


Figure A17. Prediction error boxplots for the first parameter at $61.7 \mu\text{s}$ with damage size under multiple loading states for path 2–4: (a) the no-loading condition, (b) the 5-kN case, (c) the 10-kN case, and (d) the 15-kN case.

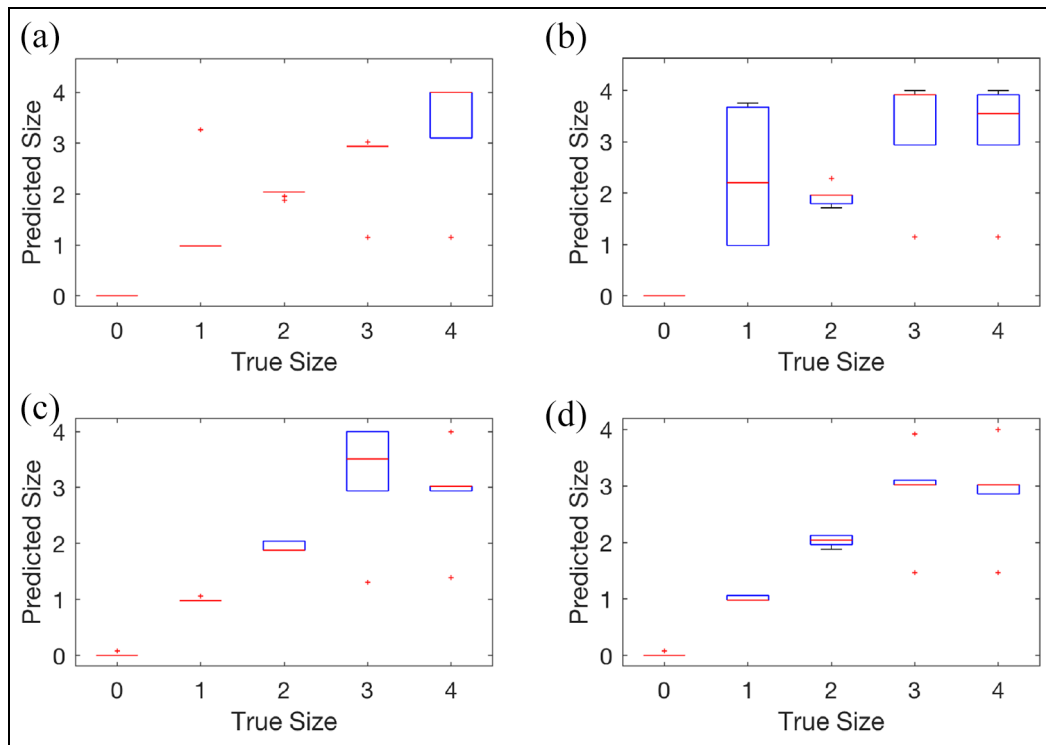


Figure A18. Prediction error boxplots for the fourth parameter at $61.7 \mu\text{s}$ with damage size under multiple loading states for path 2–4: (a) the no-loading condition, (b) the 5-kN case, (c) the 10-kN case; and (d) the 15-kN case.